Electrochemical Investigation of Microsecond Plasma-in-Liquid Treated Copper Surfaces

Master Thesis

in the Degree Program Master of Science in Physics

at the Faculty of Physics and Astronomy of the
Ruhr-Universität Bochum

by
Neil Dominik Unteregge

from
Essen

Bochum 2025

Abstract

The aim of this project is to investigate the plasma-based production of hydrogen peroxide and its effects on copper surfaces. Copper surfaces modified with hydrogen peroxide are capable of growing copper oxide crystals, which are byproducts of the oxidation of copper. Oxidized copper surfaces are valuable catalysts for the electrochemical reduction of CO_2. In this thesis an in liquid plasma is ignited in distilled water, which dissociates the water into many reactive species with different lifetimes. These are hydrogen peroxide H_2O_2, molecular oxygen O_2, and solvated electrons e^-. The plasma is ignited by microsecond voltage pulses with a maximum voltage of up to 20 kV. The concentration of hydrogen peroxide in the plasma activated water (PAW) is determined by absorption spectroscopy using ammonium metavanadate as a binder. Afterwards, the PAW is used to oxidize the copper surfaces. Finally, the copper surface is analyzed using cyclic voltammetry, to determine the quality of reduction in terms of copper crystals grown. In addition, the treated copper surfaces are being analyzed using scanning electron microscopes, to observe and visualize the copper crystals.

Zusammenfassung

Das Ziel dieser These ist die Analyse der plasma-basierten Produktion von Wasserstoff peroxid und deren Wirkung auf Kupferoberflächen. Die Behandlung der Kupferoberfläche durch Wasserstoff peroxid verursacht den Wachstum von Kupferoxid Kristallen, welche ein Nebenprodukt der Oxidierung des Kupfers sind. Oxidierte Kupferoberflächen sind wertvolle Katalysatoren für die Elektrochemische Reduktion von CO_2. In dieser These wird ein Plasma in destiliertem Wasser gezündet, was dazu führt, dass das Wasser in viele verschiedene Spezies mit verschiedenen Lebensdauern dissoziiert. Spezies sind Wasserstoff peroxide H_2O_2, molekularer Sauerstoff O_2 und gelöste Elektronen e^-. Das Plasma wird gezündet mit einem Mikrosekunden Spannungspuls mit einem Maximum von 20 kV. Die entstehende Wasserstoff peroxidkonzentration in dem Plasma aktivierten Wasser (PAW) wird ermittelt durch Absorptionsspektroskopie unter Verwendung von Ammonium Metavanadat als Bindungsmittel. Danach wird das PAW benutzt, um die Kupferoberflächen zu oxidieren. Zum Schluss werden die behandelten Oberflächen mit Hilfe von Cyclovoltammetrie analysiert, dabei wird die Qualität der Oxidation auf der Oberfläche ermittelt. Zusätzlich werden die behandelten Oberflächen mithilfe eines Rasterelektronenmikroskops analysiert, um die Kupferkristalle zu visualisieren.

Contents

1 Introduction **1**
1.1 Motivation . . . 1
1.2 Goal . . . 1

2 Fundamentals **3**
2.1 In liquid plasma . . . 3
2.1.1 In liquid plasma setups . . . 3
2.1.2 Examination of discharge process in liquid . . . 3
2.1.3 Comparison between atmospheric plasma discharges and in liquid discharges . . . 4
2.2 Interaction between hydrogen peroxide and copper surfaces . . . 6
2.2.1 Model on interaction of hydrogen peroxide on copper surface . . . 6
2.2.2 Model for crystal growth on copper surfaces . . . 7
2.3 Crystallization and crystal growth mechanism . . . 8
2.3.1 Reactions taking place with crystal growth . . . 8
2.4 Cyclic voltammetry . . . 9
2.4.1 Fundamentals of cyclic voltammetry . . . 9
2.5 Absorption spectroscopy . . . 9
2.6 Scanning Electron Microscope (SEM) . . . 10
2.7 Magnetron Sputtering Plasma . . . 12
2.8 Rogowski coil . . . 13

3 Experimental setup **15**
3.1 Plasma chamber . . . 15
3.2 Cyclic voltammetry setup . . . 17
3.3 Absorption spectroscopy setup . . . 18
3.4 High-Power Impulse Magnetron Sputtering (HiPIMS) chamber . . . 19

4 Measurement Procedure **21**
4.1 Sample preparation . . . 21
4.2 Coating of the sample in the HiPIMS chamber . . . 22
4.2.1 Setup and procedure . . . 22
4.2.2 Coating acquisition on sample . . . 22
4.3 Preparing in liquid plasma chamber setup . . . 23
4.3.1 Electrical setup and chamber specifications . . . 23
4.3.2 Glass socket . . . 23
4.3.3 Cannula holding the electrode . . . 24
4.3.4 Tungsten wire electrode . . . 24

4.4 Plasma discharge in distilled water . . . 25
4.4.1 Ignition and initiation specifications . . . 26
4.5 Copper treatment with Plasma activated liquid . . . 26
4.5.1 Treatment of copper surface . . . 26
4.6 Analyzing the copper surface using cyclic voltammetry . . . 27

5 Results, analysis and discussion **29**
5.1 Treatment of liquid . . . 29
5.2 Discussion of data . . . 29
5.2.1 Frequency generator, voltage and current graph . . . 29
5.2.2 Power and energy graph . . . 31
5.3 Recording of electrical parameters . . . 31
5.3.1 Voltage variation as a function of time . . . 32
5.3.2 Current as a function of time . . . 33
5.3.3 Power as a function of time . . . 34
5.3.4 Energy as a function of time . . . 35
5.3.5 Resistance . . . 39
5.4 Measuring and evaluating temperature, concentration and conductivity 40
5.4.1 Measuring temperature . . . 41
5.4.2 Measuring hydrogen peroxide concentration . . . 43
5.4.3 Measuring conductivity . . . 47
5.5 Cyclic voltammetry . . . 48
5.6 Scanning Electron Microscope results . . . 51

6 Conclusion **57**
6.1 Outlook . . . 59

Danksagung **61**

Literature **63**

1 Introduction

1.1 Motivation

This thesis focuses on analyzing the plasma-in-liquid based hydrogen peroxide production and their oxidizing capabilities on copper surfaces. The motivation behind using microsecond pulsed plasmas instead of nanosecond pulsed plasmas is to better understand the effect of prolonged discharge times in the liquid, assuming, that the conversion rate is directly dependent on energy dissipation. Oxidized copper surfaces function as catalysts and are very valuable in many research topics in science. The microsecond plasma based water treatment of copper surfaces functions as an efficient method of obtaining these catalysts. Catalysts are a tool used to perform a reaction that is otherwise difficult to achieve, for example the conversion of carbon dioxide CO_2 into other multicarbon products[1]. This is especially interesting, because today the climate change is a worldwide problem, which is mainly due to greenhouse gases like CO_2 in the atmosphere.
In the last few decades, the demand for energy has increased, which had the following consequence of increased fuel usage, which poses two critical problems, first is the ongoing depletion of fossil fuel energy sources and secondly the air pollution and climate change due to emission of greenhouse gases. A possibility to alleviate the problem would be the use of copper catalysts in photocatalytic CO_2 conversion into multicarbon products and water splitting[1][2]. This would reduce the amount of greenhouse gases and increase the resource of carbon neutral energy sources. Despite the fact, that copper based materials have been investigated for decades, there are still numerous challenges on the path to fundamental understanding and large scale deployment of copper based electrocatalysts for CO_2 reduction.

1.2 Goal

The goal of this thesis is to further understand the mechanics in hydrogen peroxide generation using microsecond pulsed plasmas and their oxidizing effect on copper surfaces. Using a microsecond pulsed plasma reveals potential differences in hydrogen peroxide production in contrast to the nanosecond pulsed plasmas. The dependence of hydrogen peroxide production is not strictly limited to the parameters analyzed in this thesis. The oxidizing agent used to treat the copper surface is predominantly hydrogen peroxide. Yet as the dissociation in liquid produces more radical species than hydrogen peroxide, appropriate attention on the analysis of electrical parameters is needed. This is done by recording every crucial parameter of the microsecond pulsed plasma, as well as a cyclic voltammetric analysis of the treated surface and scanning electron microscope images of the treated surface for visualization. Correlating the

results gives a comprehensive assignment of the behavior of the many parameters and how they are linked to one another.

2 Fundamentals

In this thesis, the effect of hydrogen peroxide on copper surfaces is analyzed using cyclic voltammetry, absorption spectroscopy and scanning electron microscopy. A suitable method of obtaining hydrogen peroxide is to break down distilled water using in liquid plasma. Therefore, an overall fundamental understanding of in liquid plasmas is required. This section provides the required theoretical background for the different processes.

2.1 In liquid plasma

2.1.1 In liquid plasma setups

Ignition of plasmas in liquid is different, compared to ignition in any gas or environment with low pressure. In liquid plasma setups, there is a variety of different configurations. Prominent examples would be pin-to-plate or pin-to-pin configurations [3]. The most common configuration is a pin-to-plate configuration in which the plasma is ignited in the gas above the liquid and the liquid acts as the counter electrode. The setup used in this thesis is a pin-to-pin configuration, where the ignition is fully submerged in liquid.

2.1.2 Examination of discharge process in liquid

The main type of plasma used in the production of hydrogen peroxide in liquid, are streamer discharges inside gas bubbles, which are produced by the heating of the electrodes. As the discharge takes place in liquid, the ignition conditions are different from ignitions in gas. The density in a liquid is greater than the density of air. For an ignition to take place under these circumstances, the electric field must be sufficiently strong to create bubbles via heating, in which the conditions are met for the plasma to ignite[4]. This is due to the average mean free path being very short in comparison to low pressure plasmas. For a discharge to take place, the dielectric breakdown strength V_b has to be applied, which can be calculated using the Paschen law:

$$V_b = \frac{p \cdot d \cdot B}{\ln(p \cdot d \cdot A) - \ln\left(\ln(1 + \gamma^{-1})\right)} \tag{1}$$

Where p the pressure of the medium the plasma is in, d is the electrode distance, γ the material dependent constant stating the average number of released electrons per ion and A and B being gas dependent constants[5]. At room temperature 20 K and atmospheric pressure, the dielectric breakdown strength of air is 30 $\frac{\text{kV}}{\text{cm}}$[6] and for water the dielectric breakdown strength is 650 to 700 $\frac{\text{kV}}{\text{cm}}$[6]. Section 5.1 will go into detail for the needed electric fields. These discharges can be sustained using voltages

of 50 kV up to 400 kV, drawing a current of hundreds of Amperes, varying depending of the external parameters, namely electrode distance, room temperature and water conductivity[3]. Industrially, it is difficult to maintain electrical power of this magnitude, which is why this plasma is generated using a microsecond pulsed voltage, lasting a couple microseconds. In this thesis a voltage of 20 kV and electrical current of up to 2 mA have been used. The application of these parameters ensures an electric field capable of generating self propagating ionization waves[4]. There are some theories on how a plasma can generate in liquid at the given parameters of 20 kV and 2 mA. The most probable explanation is that for a streamer discharge in liquid to take place, a bubble at the surface of the electrode has to be formed. This bubble is most likely formed by ohmic heating in the water in the vicinity of the electrode tip[3], which will in turn create a water vapor bubble, in which the conditions for plasma are more favorable[7][8], as seen in Fig. 1. Bubbles usually form after 1 µs and have sizes between 40 to 100 µm considering the parameters used in this thesis. The bubbles are therefore called microbubbles [8]. The streamers propagate at a velocity of 20 to 100 mm μs^{-1}. The streamer, consisting of an ionizing wave will reach a liquid gas interface inside the bubble, it will penetrate the liquid to a lesser extent and cause impact ionization, as well as dissociation inside the liquid. The liquid has a higher density than the gas inside the bubble, therefore the ionizing wave will quickly lose its built up energy inside the liquid via collisions[3].

Figure 1 shows an illustration of bubbles forming and subsequent plasma discharge inside the bubbles. The initial state of the liquid surrounding the electrode right after applying the electric field is fluctuating. After a short delay, the liquid starts to heat and evaporate near the electrode. This in turn will create a micro bubble. Enough micro bubbles will form until a path is formed, in which the ionization wave can protrude into the liquid. After multiple protrusions, a gas channel will form, where the dissociation degree is high and plasma can form more easily. Depending on the length of the applied electric field, multiple discharges can be formed within a single pulse.

2.1.3 Comparison between atmospheric plasma discharges and in liquid discharges

Because of the change in parameters inside the bubble, a discharge can more easily form inside the less dense material. This discharge can carry charges in a streamer like propagating manner along the bubble onto the liquid gas interface. The ionized particles will accelerate and collide with the surrounding liquid, initializing impact and ionization and dissociation, which in turn will produce the long and short lived reactive species. A comprehensive list of the species created is shown in figure 2.

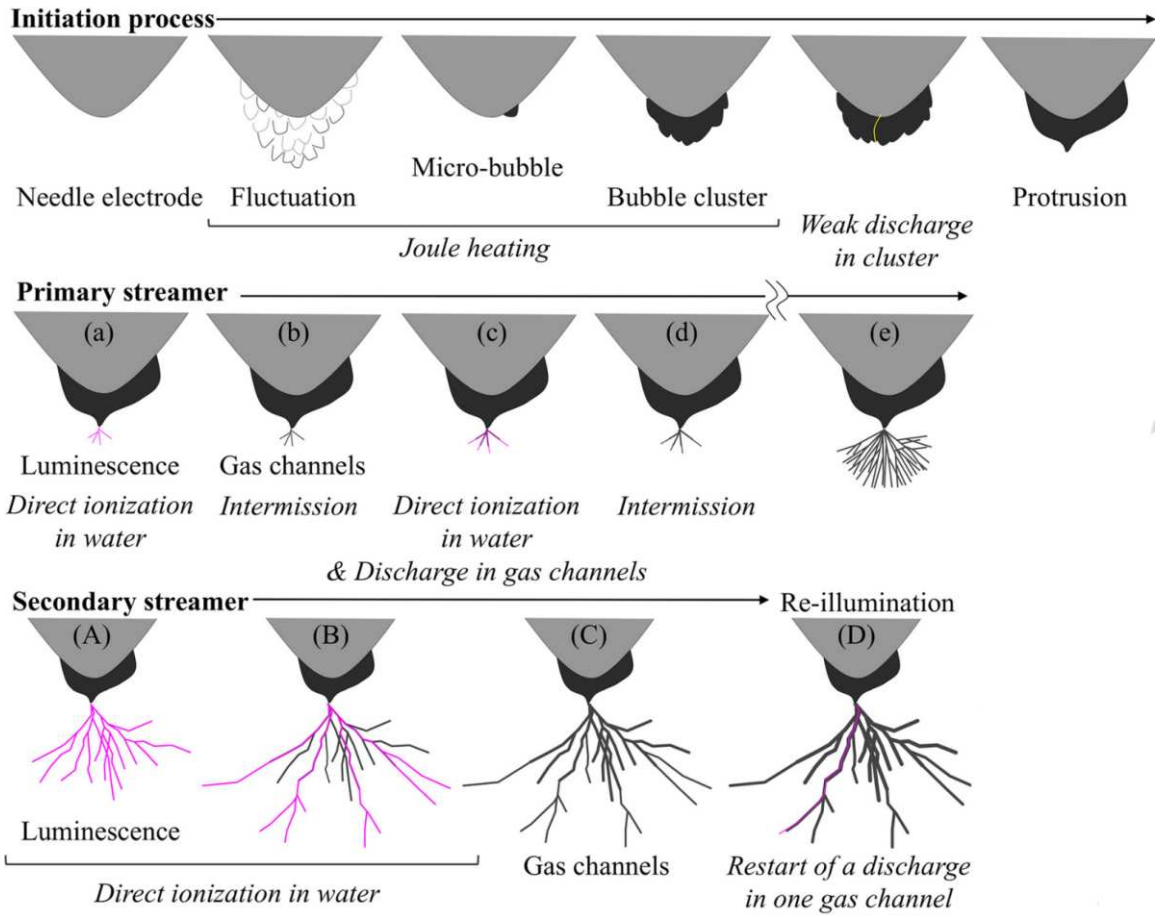

Figure 1: Bubble formation and subsequent plasma ignition in liquid via microsecond pulsed discharges, from [9].

.

The significant reactions listed are the impact dissociation of H_2O into OH^- and H^+ and the reaction of 2HO into H_2O_2. Any reaction producing OH^- and not destroying H_2O_2 will contribute to the generation of H_2O_2. Every other reaction listed is not significant in the generation of H_2O_2, but they represent other volatile species created during a discharge in H_2O, which may have unwanted side effects, such as reducing or oxidizing capabilities, which may impact the surface.

As the distilled water is stored in air atmosphere, it will dissolve the components of air, mainly 78 % nitrogen, 21 % oxygen, 0.9 % argon and 0.1 % residual gases[11]. The only relevant changes by solvation is nitrogen, yet it will not alter the discharge in regards to the hydrogen peroxide generation. As the nitrogen is dissolved and contained in the solution, reactive nitrogen species will be generated in the discharge. This can affect the application of the plasma treated water, as reactive species have oxidizing and reducing capabilities, which can alter the data collected in cyclic voltammetry, which is discussed in Section 4.6.

$$H_2O + e \rightarrow OH\bullet + H\bullet + e^-$$
$$H_2O + e \rightarrow H^+ + OH\bullet + 2\,e^-$$
$$H_2O + e \rightarrow H\bullet + O\bullet + H\bullet + e^-$$
$$O_2 + e \rightarrow O^+ + O + 2e$$
$$O_2 + e \rightarrow O^- + O$$
$$O + O_2 \rightarrow O_3$$
$$O_3 + NO \rightarrow NO_2 + O_2$$
$$N + O_2 \rightarrow NO + O$$
$$O + N_2 \rightarrow NO + N$$
$$O + NO_2 \rightarrow NO + O_2$$
$$2\,NO + O_2 \rightarrow 2NO_2$$
$$NO_2 + OH \rightarrow HNO_3$$
$$H_2O_2 + h\nu \rightarrow OH\bullet + OH\bullet$$
$$3\,NO_2 + H_2O \rightarrow 2\,HNO_3 + NO$$
$$H_2O_2 + H^+ + NO_2^- \rightarrow ONOOH + H_2O$$
$$OH\bullet + OH\bullet \rightarrow H_2O_2$$
$$NO + NO \rightarrow N_2 + O_2$$
$$NO + OH\bullet \rightarrow HNO_2$$
$$HNO_2 + OH\bullet \rightarrow NO_2 + H_2O$$
$$NO_2 + h\nu \rightarrow NO + O\bullet$$
$$NO_3 + h\nu \rightarrow NO + O_2$$
$$NO_2 + NO_3 \rightarrow N_2O_5$$
$$N_2O_5 + H_2O \rightarrow 2HNO_3$$
$$2\,NO_2 + H_2O \rightarrow NO_2^- + NO_3^- + 2H^+$$
$$3\,NO_2^- + 3\,H^+ \rightarrow 2\,NO + NO_3^- + H_3O^+$$
$$OH + NO_2 \rightarrow [O{=}N{-}OOH] \rightarrow O{=}N{-}OO^- + H^+$$

Figure 2: A list of reactive species created by the in liquid discharge with 20 kV voltage, from [10].

2.2 Interaction between hydrogen peroxide and copper surfaces

2.2.1 Model on interaction of hydrogen peroxide on copper surface

An universal model of the interactions of aqueous solutions on copper surfaces has not yet been developed. Therefore, each individual contact of a solution with the specified material has to be predicted by models. In this thesis, a model of the interaction of hydrogen peroxide with copper and the resulting growth of crystals by DeNardis et. al.[12][13] is considered. This model was created in order to incorporate the different alterations of the copper surface. It is based on the research of N. Cabrera et. al.[14] and was modified to represent the interaction of hydrogen peroxide solutions on copper surfaces. The mechanism discussed in the paper is the copper chemical mechanical planarization (CMP), which has become an effective method of achieving local and global planarity across a wafer[12]. It covers removal and growth rates of oxide crystals

on copper. This thesis addresses the growth processes, as the removal is well understood as part of the planarization process.

2.2.2 Model for crystal growth on copper surfaces

An aqueous solution with oxidizing components induces oxide crystal growth on copper surfaces[12]. This model of copper oxidation is developed based on cation migration[13]. The unoxidized Cu^0 in the bulk of the volume has an interface to the surface area, at which oxidizing agents are going to attach to. This establishes the interface between the copper and other solutions. This interface consists of oxidants, which are likely to be absorbed by the copper. After formation of a thin film of oxidants at the copper surface, the oxidants will begin to attract electrons from the copper bulk, causing a flow of electrons into the film[12]. This electron flow is sufficiently stable to ensure that some of the copper bulk species become cations and some of the absorbed oxidants become anions. The separation of charges develops a potential difference and therefore an electric field, which impacts the anions in the bulk to drift normal to the interface. In order for an anion to move, it has to have sufficient energy to surpass a certain energy threshold[13]. This energy is composed of the bonding energy of copper substrate atoms within the bulk and the energy required for copper anions to bind to the oxide. The sum of the energies for an anion in the copper bulk to move and bind to an oxidant is summarized as W. Therefore, we can determine the probability rate p in Hz, for an ion to move and bind to an oxide per second, to be:

$$p = f \cdot \exp\left(-\frac{W}{k_B T} + \frac{qaE}{2k_B T}\right) \tag{2}$$

In this equation, f represents the frequency of atomic vibrations, k_B is the Boltzmann constant, T is the temperature at the interface, q is the charge of a proton, a represents the lattice constant of Cu_2O and E is the induced electric field. The exponent contains two parts: The first part represents the energy an ion needs to receive to overcome the potential barrier and the second part represents the energy an ion receives from the induced electric field. One can now rewrite the equation to relate to the growth rate of oxide$\frac{dx}{dt}$ as follows:

$$\frac{dx}{dt} = N\Omega f \exp\left(-\frac{W}{kT}\right) \exp\left(\frac{qa}{2kT}\frac{V}{x}\right) \tag{3}$$

Here, N represents the number of cations per unit area and Ω represents the volume of oxide formed per cation. The product $N\Omega f$ is assumed to be $10^4\,\mathrm{cm/s}$[12]. The energy W is dependent on temperature and is determined to be around $0.83 - 0.85\,eV$ at $25 - 60\,°C$[13]. This model predicts, that the oxide growth rate is dependent on the

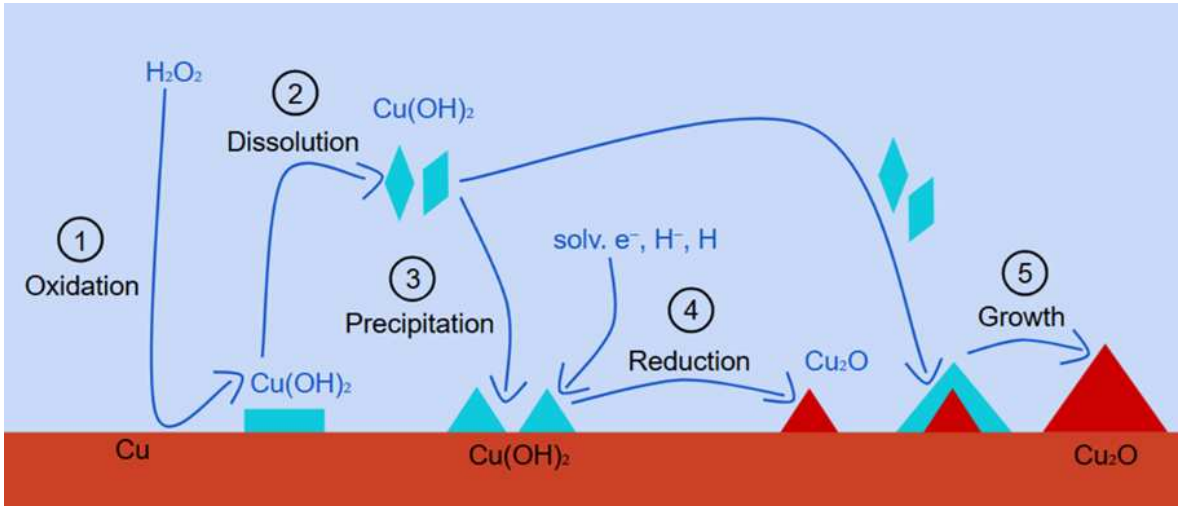

Figure 3: Illustration of the crystallization mechanism of the hydrogen peroxide on the copper interface.

already accumulated oxide thickness, the temperature and the energy W, where one can see, that the growth rates in the early instances of oxidization are up to $100000 \text{Å}/m^{-1}$ at $x_{Thickness} = 5\,\text{Å}$, exponentially falling off to $100\,\text{Å}/m^{-1}$ at $x_{Thickness} = 17\,\text{Å}$[13].

2.3 Crystallization and crystal growth mechanism

Having understood the oxidization mechanism of the bulk of copper at the interface, one can start to analyze the crystal growth mechanism induced by hydrogen peroxide on copper surfaces. The hydrogen peroxide used in this thesis is contained within distilled water, it is therefore an aqueous solution.

2.3.1 Reactions taking place with crystal growth

When the aqueous solution containing hydrogen peroxide comes in contact with the copper surface, a thin film of oxidants will attach to copper. Figure 3 is an illustration of the copper oxides forming on the surface. With time, copper will be oxidized into $Cu(OH)_2$ by H_2O_2, which will dissolve into the solution. The dissoluted $Cu(OH)_2$ will precipitate back onto the copper surface, where it will be reduced via solvated electrons, H or H^- into Cu_2O. The Cu_2O is strongly bonded to the copper surface and provides an advantageous interface for $Cu(OH)_2$ bonding, as Cu_2O has different bonding energies than the copper surface. This favors growth onto already existing crystals, which is why the crystals favor to not grow evenly distributed over the surface[13]. As $Cu(OH)_2$ has oxidizing properties, one can verify their existence using cyclic voltammetry, which will be explained in the next chapter.

2.4 Cyclic voltammetry

Cyclic voltammetry (CV) is probably the most versatile electrochemical analyzing technique used in the study of electroactive species. Its adaptability combined with ease of measurement has resulted in extensive use of CV in the fields of electrochemistry, inorganic chemistry, organic chemistry, and biochemistry[15]. Cyclic voltammetry is often the first experiment performed in an electrochemical study of a compound, a biological material, or an electrode surface. The effectiveness of CV results from its capability for rapidly observing the redox behavior of the chosen sample over a wide potential range. The resulting voltammogram is a spectrum which conveys information as a function of the redox potential scan.

2.4.1 Fundamentals of cyclic voltammetry

The method of CV is performed by applying a variable potential at an electrode, which is submerged in a conducting solution, a so called electrolyte. This potential is controlled against a reference electrode. The current measured at the working electrode is considered the response signal. Varying the potential will scan a certain potential region multiple times. Applying the potential to the surface, its composition changes. For example, the oxidized compounds will be reduced back into its original states, which will lead to a current measured at the electrode. Collecting the current measured against the voltage applied, we get a cyclic voltammogram, as seen in Fig. 4.

Figure 4 is a representation of a cyclic voltammetric scan for an electrode with different treatment times of the copper surface. Based on the value of the measured currents we can evaluate the composition of the surface. Each reaction starts at different potentials[16]. Cupric oxide (CuO) has its reduction peak at -0.47 V, the amorphous cuprite $(Cu_2O)_{am}$ has its reduction peak at -0.6 V, intermediate cuprite $(Cu_2O)_{im}$ has its reduction peak at -0.8 V and crystalline cuprite $(Cu_2O)_{am}$ has its peak at -1 V[16].

2.5 Absorption spectroscopy

In order to determine the hydrogen peroxide concentration produced by the plasma, absorption spectroscopy was used. Hydrogen peroxide absorbs ultraviolet light with a wavelength of about 200 nm to 400 nm [17],[18]. A 30% hydrogen peroxide solution is used to produce several solutions with different concentrations of hydrogen peroxide by dilution. These are used to create a calibration curve for sample fitting. Spectroscopy at low wavenumbers can lead to inaccuracies in detection and a large range of absorption

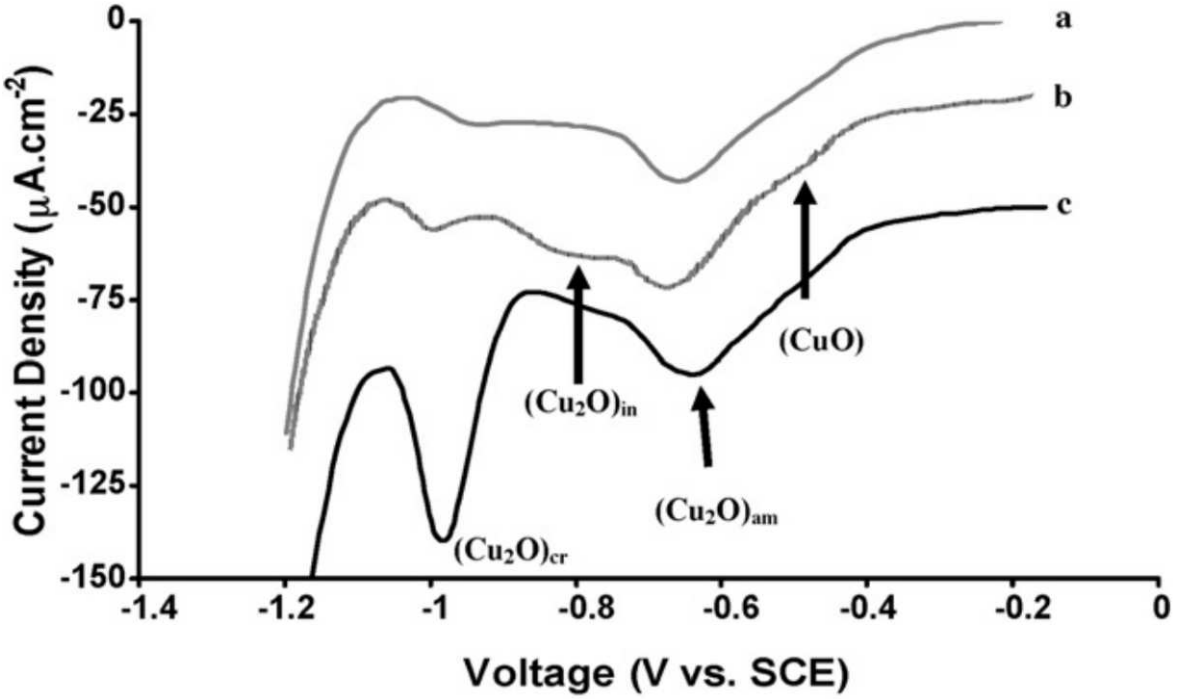

Figure 4: Potentiodynamic curves of copper in deaerated 0.1 M KCl solution after exposure to 800 ppb acetic acid at 95% RH for 7 days (a), 14 days (b), and 21 days (c) with a scan rate of 1mV/s, from [16].

wavelengths also makes detection more difficult. Therefore ammonium metavanadate solution was applied to the samples. The reaction of hydrogen peroxide with ammonium metavanadate results in a red to orange peroxovanadium cation solution, which shifts the absorption region from 200-300 nm to a peak at 450 nm. The absorption of the compound is proportional to the hydrogen peroxide concentration and follows Beer-Lambert Law:

$$I = I_0 e^{-\epsilon c d} \tag{4}$$

where I is the measured Intensity, I_0 is the reference intensity, ϵ is the absorptivity, d is the absorption length and c is the to be determined concentration of the analyzed solution. The lower detection limit of this spectrophotometric method was found to be 143 µM[19].

2.6 Scanning Electron Microscope (SEM)

Scanning electron microscope (SEM) is one of the most multifaceted and versatile instruments available for the analysis and examination of the microstructure. It is necessary to know the basic principles of light optics in order to understand the fundamentals of electron microscopy.

The scanning electron microscope operates, in contrast to common microscopes, with the detection of electrons. As microscopes detect reflected light from the object, one can analyze the interface with many wavelengths of light, therefore receiving information of the contour of the surface. Yet light has a distinct drawback, because its wavelength will be as large or lager than the objects on the surface. As visible light has a wavelength of 300 nm up to 800 nm, it can only accurately depict objects slightly larger than the wavelength used to analyze it. Objects as large as the wavelength will scatter the wave, as Mie-scattering. Mie-scattering takes place, when objects as large as the wave might elastically scatter upon collision with the small object. This in turn will make small objects hardly representable, as the light will not correctly reflect back into the detector of the microscope. The small object will get blurred and no clear information can be obtained. This is why an electron microscope has advantage over common microscopes. As the SEM uses electrons as the analyzing media, it will have far greater resolution. This is due to the wavelength of the electron proposed by de Broglie, which is dependent on its energy:

$$\lambda = \frac{h}{p_e} = \frac{h}{\sqrt{2m_e E_{kin,e}}} \tag{5}$$

Where h is the planck constant, p_e is the momentum of the electron, m_e is the mass of the electron and $E_{kin,e}$ is the kinetic energy of the electron.
The energy the electron receives in the scanning electron microscope is usually 10 keV up to 20 keV [20]. This means the electron has a de-Broglie wavelength of $1.226 * 10^{-11}$ m or $8.672 * 10^{-12}$ m respectively. In other words the electron has a de-Broglie wavelength of about 8.7 pm to 12.3 pm, which is far smaller than visible light with 300 nm. It is a factor 10^4 times smaller than visible light, which also indicates better resolution.
The scanning electron microscope is built as depicted in Figure 5.
It is composed of many different parts. First we have the source of electrons named "electron gun", named in Figure 5. It is a component which emits electrons via thermic emission. These electrons are being accelerated by an electric field and are formed into an electron beam. As the electrons are being drawn into the beam, they will reach a focus point, at which the electrons start to spread across as they move along the optical path. This so called beam spread is being counteracted by many electromagnetic lenses to focus the electron beam back onto a small area. With the last lens aperture, the beam is focused onto an area about 0.5 nm to 5 nm [21] on the sample. The electrons interact with the sample, performing elastic collisions. This results in the electrons being reflected by the material, ionizing atoms in the material or being trapped inside the material. This also results in detectable secondary electron emission, back scattered electrons, characteristic atomic emission spectra and light [21], which are picked up

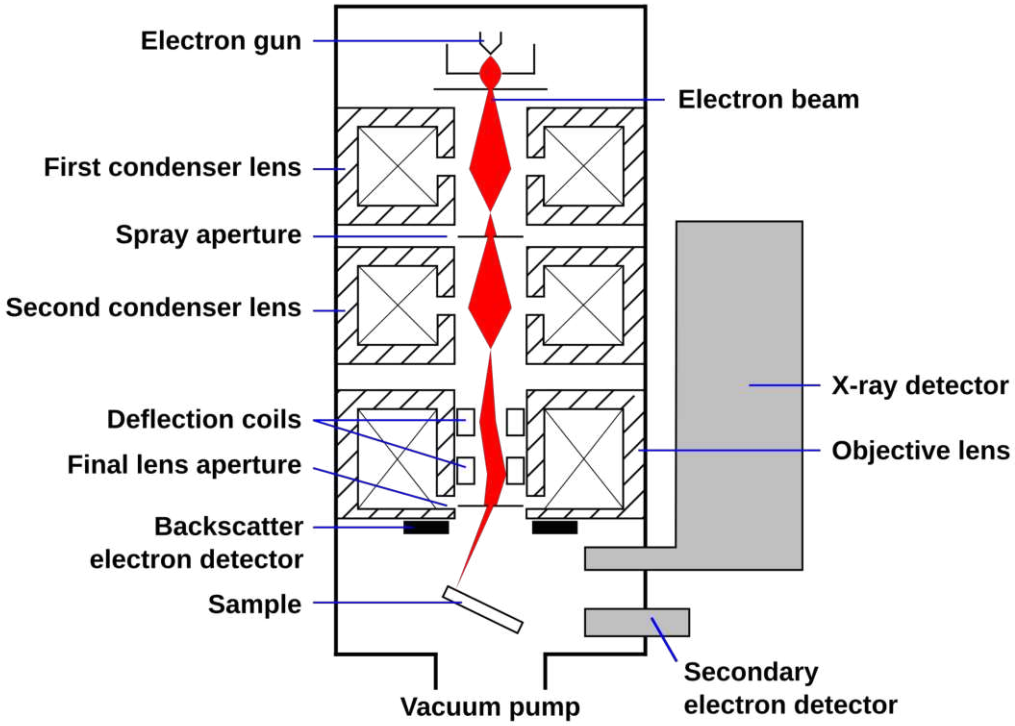

Figure 5: Setup of a scanning electron miscroscope with trajectory of electrons inside the chamber, parts are not to scale, derived from [20].

by sensors. Scanning this process over a larger area yields a signal, which combined generates a useful photograph of the scanned space. Keeping the chamber at low pressures ensures, that as little dust or gas molecules possible are interfering with the measurement. The sample is also grounded to prevent the charges from building up at the surface, which would lead to local electric fields, which disturb the scanning process.

2.7 Magnetron Sputtering Plasma

The process of magnetron sputtering is a plasma-based physical vapor deposition technique used to create thin films. It is used to sputter a material and scatter it into the surrounding atmosphere and onto a sample. The sputtered material forms thin layers on the surrounding areas including the sample. The parameters of the coating can be controlled precisely by adjusting the pressure of the inert gas, the time of treatment, distance from electrode to sample and bias voltage generated, through the size difference of the chamber and sample table.

Atoms in the inert gas are ionized by electrons, which are accelerated by the electric field. This creates ions, which are in turn accelerated towards the sample. The ions accumulate enough energy to sputter material from the sample. As the energetic ions interact with the atoms of the material, they perform elastic collisions and transfer

their energy onto the bound atoms. If the colliding ions have sufficient energy, more or equal to the binding potential of the atom, the atom are sputtered from the material. Cathode sputtering is an example, where an electric field is applied between two electrodes and increased adequately enough for ions to sputter the electrode. To increase the production of ions for physical sputtering, a magnetron is used. A magnetron is an arrangement of magnets, to form a magnetic field in a toroidal shape above the material to be sputtered. Now with the addition of a magnetron, the electrons produced by the plasma are trapped along magnetic field lines on a helix shaped trajectory. This reduces the loss of energetic electrons and allows for more electron collisions inside the region with the trapped electrons. The dense electron regions result in a higher degree of dissociation of the gas. Having the gas ionized by electrons, the ions will be affected by the electric field applied between the electrodes, therefore accelerating towards the material and distribute their energy via elastic collision, henceforth sputter the material.

2.8 Rogowski coil

The Rogowski coil is a device used to measure currents. The Rogowski coil is a coil, which is placed around a conductor. The basic principle of this device is based on Amperes law6, which states, that every material, that is conducting a changing current produces a magnetic field B proportional to the current strength I.

$$B = \frac{\mu_0 \cdot I}{2\pi \cdot r} \tag{6}$$

Where $\mu_0 = 4\pi \cdot 10^{-7} \frac{\mathrm{N}}{\mathrm{A}^2}$ is the permeability of free space and r is the distance from the conducting material. The change in current inside the material generates a changing magnetic field on the outside. This change in magnetic field can be registered, using induction. Electromagnetic induction states, that change in a magnetic field induces a voltage in conductors, which are perpendicular to the magnetic field lines. Therefore, if a coil is put around a conductor with changing current, a voltage can be recorded. Figure 6 shows an illustration of a Rogowski coil. Where i is the current in the conductor and v_{out} is the measured voltage.

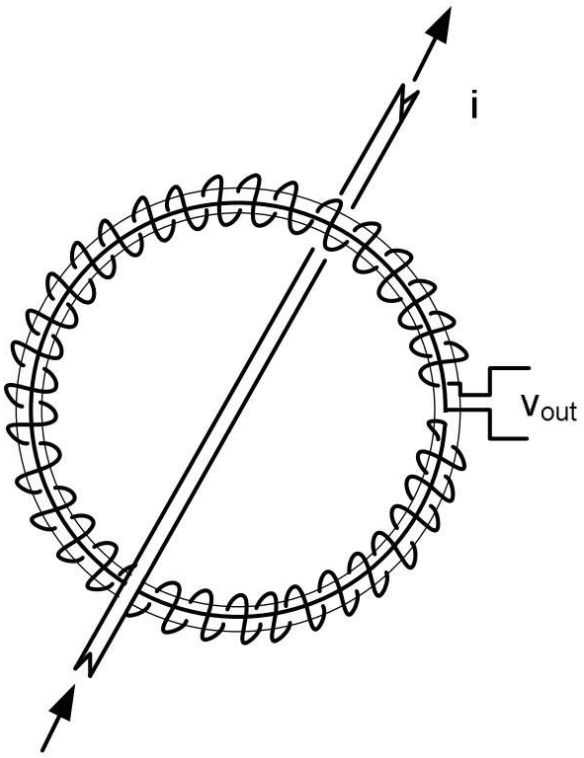

Figure 6: Illustration of a Rogowski coil, with a conductor and measured voltage

3 Experimental setup

This thesis makes use of many different setups, which will be explained in this section. It will go into detail of the different procedures and the inaccuracies. Understanding the role of each setup is crucial for interpreting the results and ensuring the accuracy and reliability of the work conducted.

3.1 Plasma chamber

The plasma chamber used in this thesis has a simple design, allowing water to flow through four different valves, enabling the content to balance the pressure inside the chamber. It has two openings for two electrodes to fit airtight into the chamber with an O-ring. The chamber accommodates a front plate containing glass for direct optical access of the discharge and a plastic backplate.
Figure 7 shows an outline of the plasma setup used in this thesis.

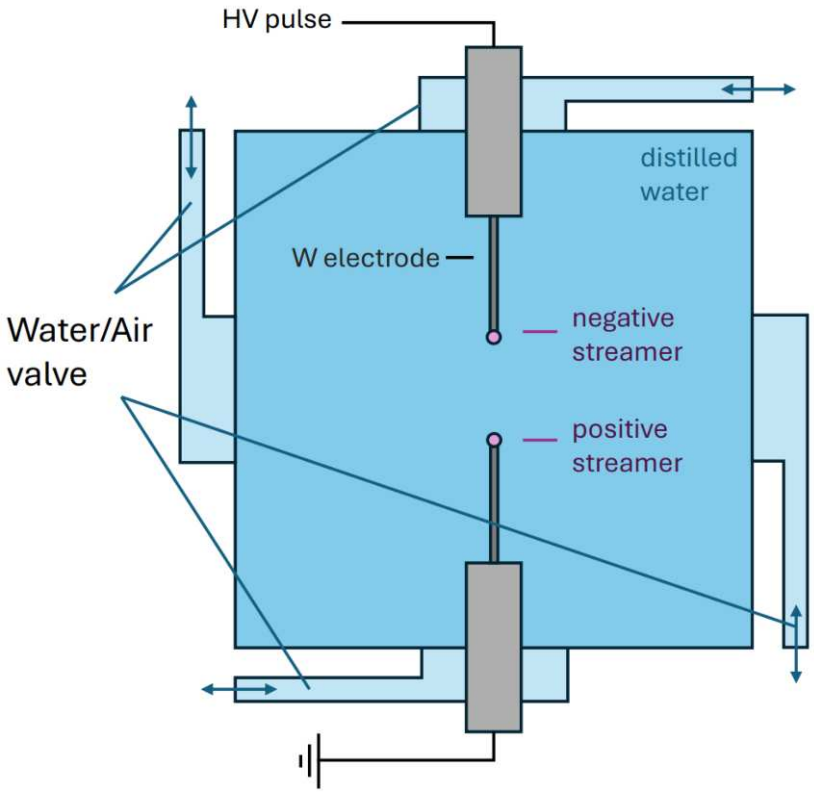

Figure 7: Outline of the plasma chamber used in this thesis, plasma dots represent the discharge.

A key feature of this chamber is to enable a flow of the liquid through the chamber, hence the four valves. Yet in this thesis it was decided for the liquid to stay stationary. The chamber can hold a maximum of up to 35 ml, but the amount used in the experiment was 30 ml to avoiding spilling of the content and ensure the option for the contents to

equilibrate its pressure while the discharge is running. The amount of liquid will affect the discharge parameters, because heat transport and conductivity will change, based on the amount of liquid used. The tungsten electrodes are chosen to have a diameter of 50 µm. It was determined, that this diameter ensures the most advantageous discharge, in terms of heat generation, degree of dissociation and local electric field[22]. The tips of the electrodes have a distance of about 1 cm. The distance between the electrodes has an impact on the dissociation of water, as for shorter distances the local electric field will be larger than if the electrodes have a greater distance. AS the electric field is great in the vicinity of the electrode, the acceleration of charged particles is also great. Thereby the particles have more energy to transfer on impact. This leads to rapid heating of the electrodes and the liquid, which is not ideal for hydrogen peroxide production. If heat is generated and the liquid is vaporized, the generated gas will take up more space than in liquid form, therefore increasing the pressure inside the chamber. To ensure that the pressure inside the chamber will not build up, at least one valve will stay open, so that the excess pressure can escape into the environment.

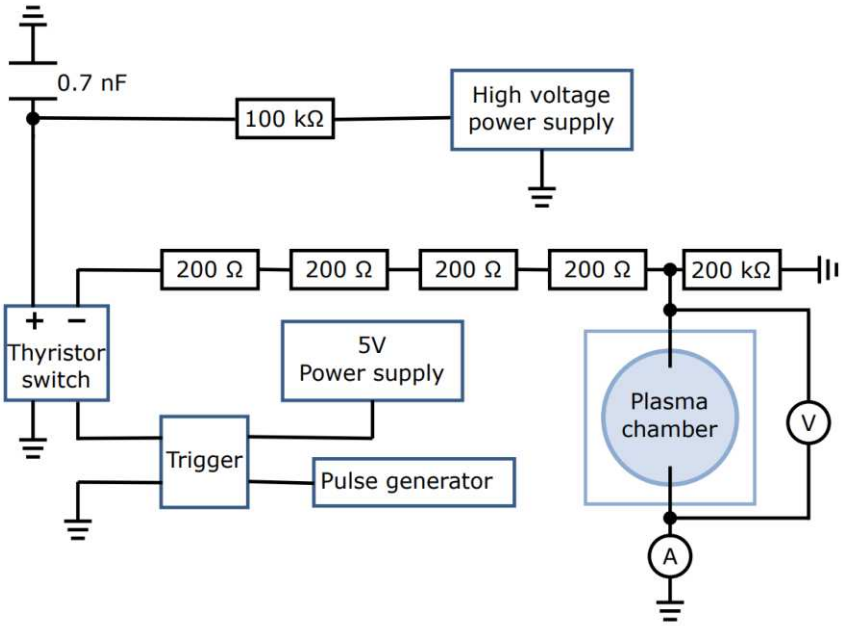

Figure 8: Schematic of the wiring of the experiment, including the trigger, the switch and the chamber, from [8].

In Figure 8 you can see the schematic overview of the wiring of the chamber. A capacitor with a capacitance of 0.7 nF is charged via a high voltage power supply. A thyristor switch sends a signal, so that the capacitor releases its charge into the powered electrode and a plasma can be ignited. This switch is controlled via a trigger, which is powered by a 5 V power supply and activated by the pulse generator. This setup allows voltages up to 30 kV. A voltmeter was installed parallel to the powered electrode to the grounded

electrode across the chamber to correctly measure the voltage applied in the chamber. Also an amperemeter was connected to the grounded wire to measure the current.

3.2 Cyclic voltammetry setup

The cyclic voltammetry setup enables the examination of the composition of a surface by application of a driving voltage and recording the subsequent current. This procedure allows the analysis of the surface reduced by the applied voltage. The strength of the measured current indicates the amount of reduced species, therefore specifying the amount contained on the surface.
Figure 9 shows a depiction of the setup used for cyclic voltammetry.

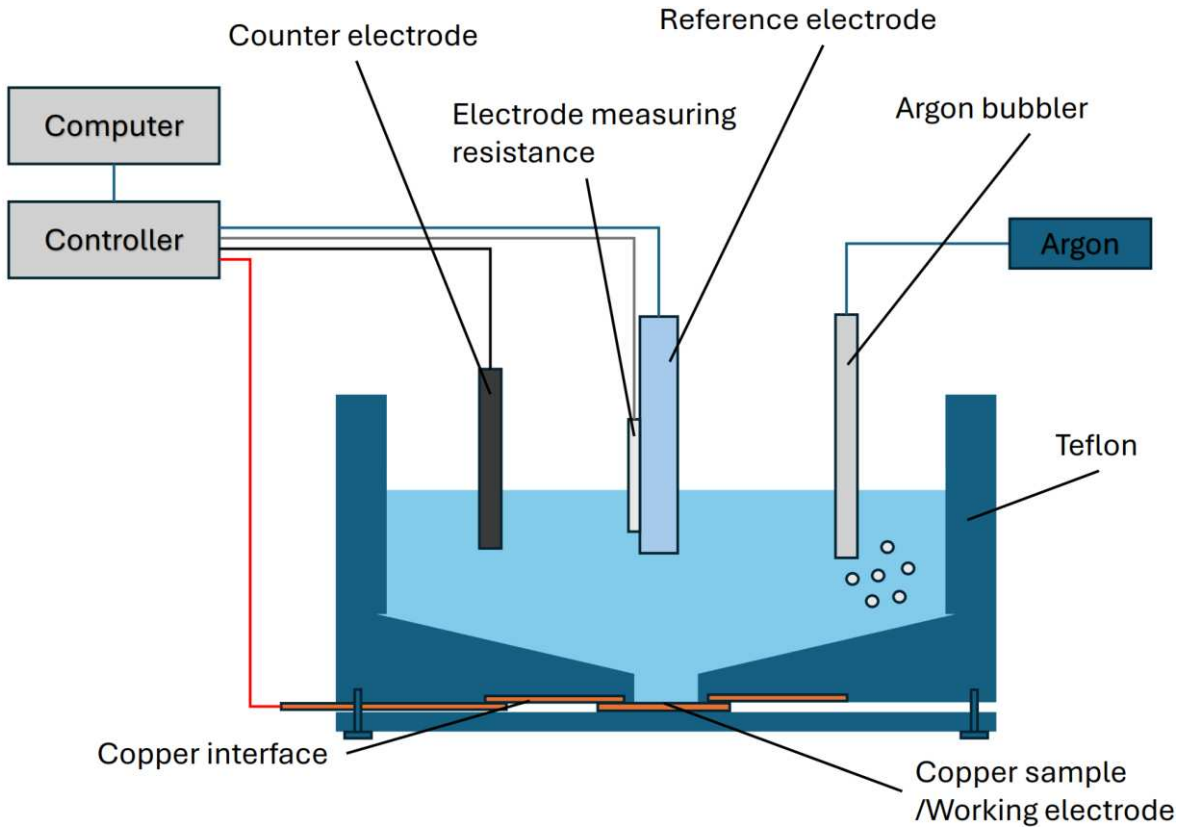

Figure 9: Illustration of the setup used for the cyclic voltammetry.

The container made of teflon can roughly hold up to 15 ml of liquid and contains the electrolyte. The electrolyte consists of 0.1 M kalium sulfate (K_2SO_4) and 0.01 M kalium hydroxide (KOH). Teflon minimizes the possibility of interaction between the solution with other materials, which helps to protect the purity of the solution and to reduce pollution. The container is open on the top side and has a small hole at the bottom side, having a sloped surface at the bottom for the liquid to accumulate in the gap as seen in Figure 9. The gap is covered by the surface of the sample to be analyzed. The

sample will be pinned onto the gap by a lid, which is held in place by screws. The bottom of the gap is covered in copper foil. The sample is big enough to cover the gap and simultaneously be in contact with the copper foil. This allows access to the copper surface to alter its potential. A wire is connected to the copper foil, so that the copper sample can operate as the driving electrode. Submerged into the liquid are three electrodes and a nozzle of the argon line for degassing. The distances between the electrodes have to be kept constant, as altering the distance may lead to different results. Yet it should be mentioned that they are sufficiently far apart so that they do not interfere with each other. The counter electrode is a small rod made out of carbon, the resistance measuring electrode is a Platinum-Iridium wire. The reference electrode is made out of glass, with a conducting plate in its center, with the surface of the electrode being submerged in the electrolyte. The argon bubbler is a small nozzle submerged in the electrolyte, connected by a tube to an argon bottle. Argon will flow out of the nozzle into the liquid. The nozzle has a small pad of styrofoam built into its orifice, to help spread out the gas flow into the liquid, preventing big bubbles from forming as these bubbles may cause disturbances. As the electrodes are connected to a computer, they are able to apply the voltage to the surface and measure the current.

3.3 Absorption spectroscopy setup

Measurement of hydrogen peroxide production was conducted via optical absorption spectroscopy. The basic absorption is described by Beer-Lambert law

$$I(c) = I_0 \cdot \exp(-\epsilon \cdot c \cdot d) \tag{7}$$

where $I(c)$ is the measured intensity of light after passing the sample, I_0 is the initial light intensity, ϵ is the absorptivity, d is the absorption length and c is the concentration of absorbing substance, in this case the absorbing substance is hydrogen peroxide. At room temperature hydrogen peroxide absorption wave lengths range from 200 to 300 nm [23].

As the range of absorption for hydrogen peroxide is broad in the ultra violet, it is more difficult to obtain a light source which can generate high frequency light in a broad spectrum.

A common approach in literature for this problem is the utilization of a binder for the hydrogen peroxide to lower the absorption wave frequency.

In this thesis the concentration of hydrogen peroxide was measured by two methods. First it was measured with an optical absorption setup and secondly it was measured with a modern measuring device designed specifically for detecting hydrogen peroxide. This machine has the same setup as the first optical absorption setup, but it is far more

precise.
For the first measurement with the optical absorption setup, ammonium metavanadate (NH_4VO_3) was used as a binder. The ammonium metavanadate will bind the hydrogen peroxide and form a red-orange peroxovanadium cation solution. This will shift the absorption range of the hydrogen peroxide from 200 to 300 nm to 450 nm. Figure 10 shows an illustration of the optical absorption setup used in this thesis.

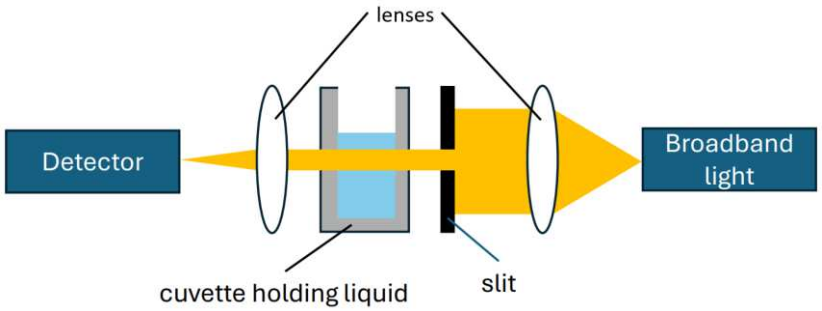

Figure 10: Optical absorption setup used,every component had to be adjusted manually, resulting in human error.

As shown in Figure 10, a broadband light source is utilized as well as two lenses, a slit, a cuvette holding the liquid and a detector. The lenses are used to collimate the light coming out of the light source and to focus the collimated light back into the detector. A slit is utilized to reduce the incoming light and block stray light sources. The light is traveling through the transparent cuvette, which is holding the sample liquid. The cuvette can hold up to 3 ml of liquid. With the light passing through the sample, the wavelengths around 450 nm will be absorbed by the compound formed by the ammonium metavanadate.

3.4 High-Power Impulse Magnetron Sputtering (HiPIMS) chamber

To obtain a copper surface, High-Power Impulse Magnetron Sputtering (HiPIMS) was used to coat silicon wafers with copper. The surface produced by the HiPIMS chamber ensures, that the present surface is even and has minimal impurities. Figure 11 shows the structure of the HiPIMS chamber used in this thesis. It is composed of a vacuum chamber with two sample holders and a target holder. The tables are connected by wires so that they can be controlled by the power supply and the computer. Argon was used in this thesis for the HiPIMS chamber. A turbo molecular pump is keeping the pressure of the chamber at small pressures, roughly 10^{-7} Pa. When the gas is introduced into the chamber, the pressure rises to about 0.5 Pa. This pressure is applied to maximize the sputtering yield, as too low pressures result in too little collision. Yet with higher pressures too many collisions result in a lower mean free path for the electrons and they can not gain enough energy to ionize the gas before they loose their energy by

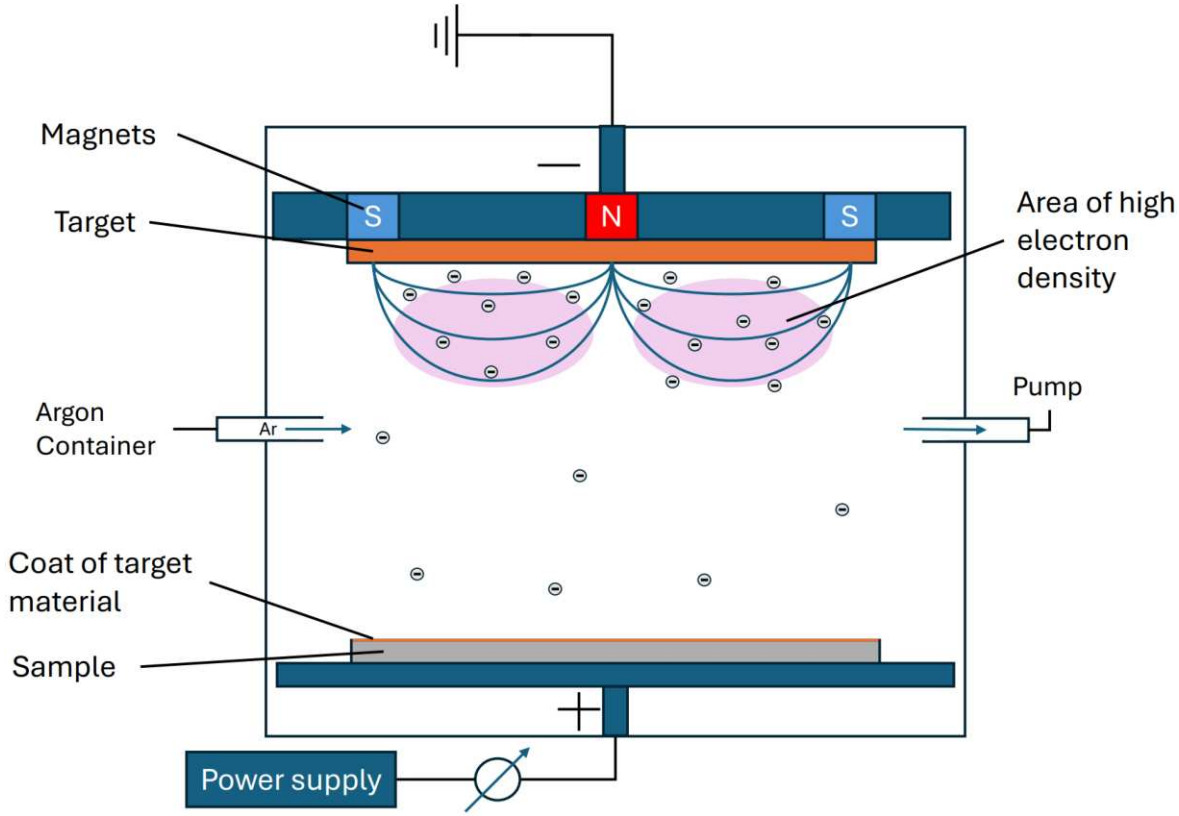

Figure 11: Sketch of the HiPIMS chamber used in this thesis.

elastic collisions. There are permanent magnets installed into the table holding the target. They are aligned to establish a toroidal field of magnetic fields in order to create areas for the electrons to be trapped and accumulate in order to obtain higher electron densities and therefore higher collision and ionization rates. To improve the degree of ionization, one wants to increase the power input, which will have some drawbacks. Some of these drawbacks include heating of the target, which may cause the target to melt and lose its form. To counteract these drawbacks the plasma will be ignited at a low frequency of 35 Hz, 740 V voltage, 110 A current, 1 kW maximum power and 50 µs pulse time.

As the gas is ionized in the plasma by the accelerating electrons, the newly formed ions will accelerate towards the surface of the target and scatter target material atoms into the chamber. The scattered atoms remain without charge and would be too heavy to be accelerated by the magnetic and electric field. As a result of the atoms being unaffected by the fields, they scatter across the whole chamber. The atoms will lose energy by collisions with other gas atoms and not reach long distances. This is why the table of the sample will be moved fairly close to the target in comparison to the chamber walls, to maximize the coating yield and planarity on the sample.

4 Measurement Procedure

The procedure of measuring the data can create irregularities with every step. Therefore it is necessary to view the steps in detail to take every possible inaccuracy into account. Some of the steps may explain certain behaviors observed later in data collection.
In the following chapters the steps of measurement procedure are explained.

4.1 Sample preparation

The first step in preparing the sample is to cut a silicon wafer into shape and coat the samples with copper. A 75 mm diameter silicon wafer is divided into roughly 9 equal big squares with 2 cm by 2 cm length of edge. This is done using a diamond cutter and a ruler, so the errors of having uncertainties at the edges is quite high. The main objective for the preparation of a sample is to obtain a sample for the cyclic voltammetry setup to analyze and to get into contact with the copper interface on the cyclic voltammetry setup.
The 75 mm diameter silicon wafer can only produce a total of 5 intact samples.
Figure 12 shows the outline of the pattern of the cuts done to the wafer.

After the incisions have been made, pressure is carefully applied to the opposite ends of the wafer for it to snap off cleanly with the least amount of irregularities.
To further enhance the usage of a single wafer one can consider using the large areas beside the existing samples. The option to cut out these imperfect samples with a missing edge almost doubles our sample yield per wafer and as the missing corners do not impact the results it is also without disadvantages.

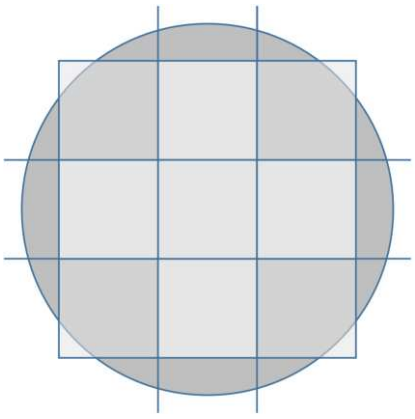

Figure 12: Sketch of a possible configuration for the cuts placed, separation occurs with breaking the wafer along the incision

4.2 Coating of the sample in the HiPIMS chamber

The coating of the sample represents a very sensitive step in the process of analyzing hydrogen peroxide production with cyclic voltammetry. If the coating is containing trace amounts of impurities, such as dust particles, the results may vary, depending on the severity of the contamination.
The process of coating a sample will be discussed in the following section.

4.2.1 Setup and procedure

The HiPIMS chamber consists of the main chamber, where the magnetron and target material are mounted, and the transfer chamber, where the sample table can be introduced and the sample can be mounted. The main chamber is evacuated by a turbo molecular pump, which can keep the pressure at about 10^{-6} Pa down to 10^{-7} Pa. The transfer chamber is evacuated by a rotary vayne pump, which can evacuate the transfer chamber from atmospheric pressures to about 10^{-5} Pa. The difference of pressures between the main and the transfer chamber is small enough for seamless transitioning of bridging the chambers as a means of opening the gate valve connecting the chambers. A long steel rod carries the table, where the sample is mounted from the transfer chamber into the main chamber. The mounting of the table in the main chamber is adjustable in height, which affects the coating yield. As the target material is being sputtered, the target atoms will propagate in all directions, which entails that the coating of the sample will have a $\sim \frac{1}{r_{dist}^2}$ dependence, where r_{dist} is the distance between the target and the sample.

4.2.2 Coating acquisition on sample

The table holding the sample has a limited area and as the coating process takes a lot of time, the area of the holding table becomes a crucial component in coating yield. To maximize the coating yield, two samples are mounted onto the table with kapton tape. After the samples have been mounted, the table is installed onto the steel rod in the transfer chamber, where the transfer chamber then gets closed and evacuated up to 10^{-5} Pa. This process can take up to 10 minutes. After the proper pressure has been reached, the gate connecting the chambers is opened for the steel rod to transfer the table from the transfer chamber into the main chamber. Retracting the rod and sealing the gate, the table is now in position for the magnetron sputtering to take place. The parameters for the magnetron sputtering discharge are chosen to be a 35 Hz frequency, 740 V voltage, 110 A current, 1 kW maximum power, 0.5 Pa pressure– and 50 µs pulse time. The table is being raised closer to the target material via a turning screw to maximize coating yield. After the coating process and after returning the table back

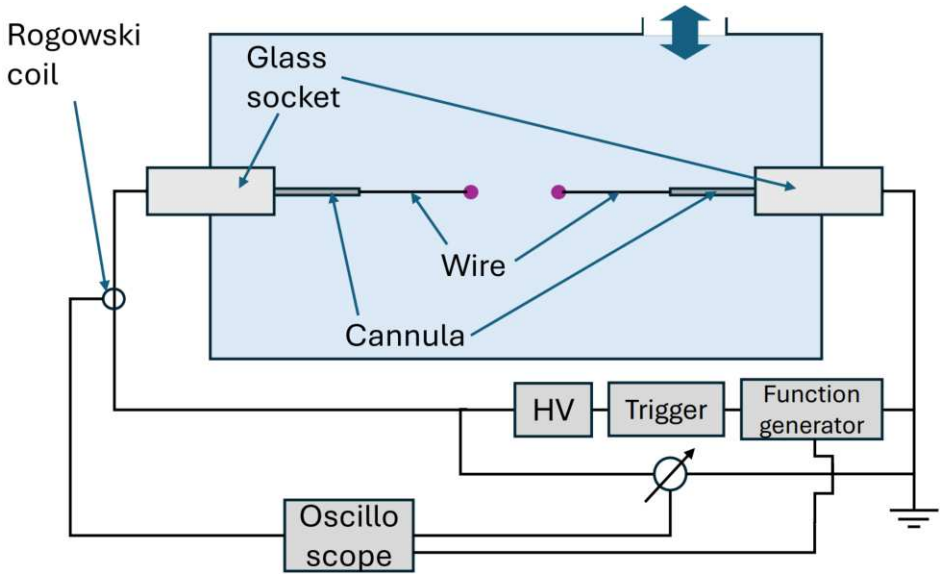

Figure 13: Optimal setup used for water treatment, showing the glass socket, cannula and wire, with the wire being straight.

into the transfer chamber, the transfer chamber gets flooded with nitrogen gas until atmospheric pressures is reached and the sample is ready to be retrieved.

4.3 Preparing in liquid plasma chamber setup

4.3.1 Electrical setup and chamber specifications

The components used for this thesis are a high voltage generator, a function generator and an oscilloscope. The chamber and therefore the liquid inside the chamber are in contact with two other materials. One is acrylic glass used for the window to observe the discharge. The other material is the back sealing plate made of polyvinyl chloride (PVC). Both materials do not interfere with the liquid inside as well as the discharge taking place inside the liquid. Figure 13 shows an illustration of the setup used for water treatment, detailing constructing parts. The preeminent factor of altering the discharge are the electrodes. For that, the electrodes will be discussed in detail. The electrodes used in this thesis are made up of three parts, which will be described in the next section.

4.3.2 Glass socket

First, there is the glass mounting socket. Figure 14 shows an illustration of the glass socket used in this thesis. This socket is made out of a glass tube which has an electrical contact at each end. On one side, it is connected to a wire that leads to the high voltage generator. The other end has a small orifice, where the electrical contact is at the inner end of the gap. This socket has the purpose to serve as an airtight connector from the

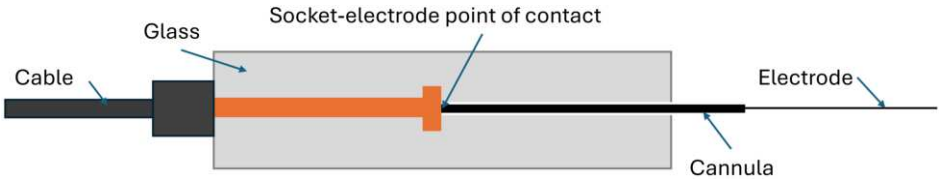

Figure 14: Illustration of the glass socket connected to a wire and holding the cannula and the electrode.

high voltage cable into the chamber. Therefore the glass tube is inserted into a small gap in the chamber which is just small enough for the insertion to be closed. There are two glass sockets inserted on opposite sites, either top and bottom or left and right. The placements of the glass socket (top and bottom, or left and right) do not have a visible significant impact on the discharge.

4.3.3 Cannula holding the electrode

The second part of the electrode is a cannula. It is a very small hollow needle, with an inner diameter of 0.4 mm and an outer diameter of 0.8 mm. It is just small enough to fit inside the gap of the glass socket of the connector from the high voltage generator. It is also long enough to get into contact with the interface of the socket, which is how the voltage is applied. The cannula gets shortened until it reaches fully into the glass socket and roughly 2 cm out of the socket. When the cannula is not mounted into the socket properly, it can easily slip and fall out of the socket. To solve this problem, a small dent is made into the cannula. This ensures, that the cannula can not be easily removed from the socket, as a sufficiently high enough force has to be applied. This force in fact is not that high, as the only force acting on the cannula would be the discharge, which is not very considerable, yet not insignificant. This concludes that the dent does not have to be great in order to stop the cannula from falling out. The sockets are inserted horizontally into the chamber. This is to prevent the undesirable unwanted dismantling of the electrodes, caused by gravitational pull on the cannula.

4.3.4 Tungsten wire electrode

The third part of the electrode is the electrode wire itself. It is chosen to be a tungsten wire with a diameter of 50 µm, as tungsten is a material with one of the highest melting points at 3695 K, as the discharge can cause local heating of several thousands of Kelvins, depending on the applied parameters and materials used[24]. The mounting of the wire into the cannula is performed by inserting the wire into the cannula and compressing the end of the cannula so that the wire is retained. The wire itself is stored in a circular tube, where it is rolled up around the cylinder. This poses an obstacle, as the wire is not straight when it is taken out of storage. The wire can not easily be straightened

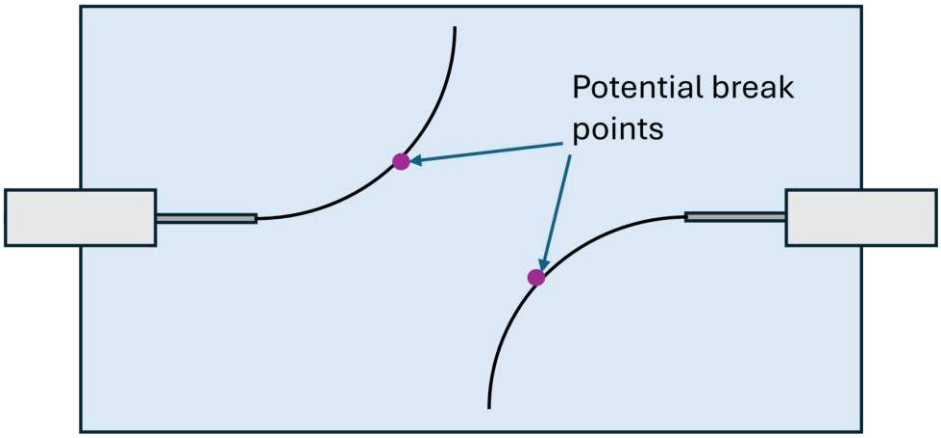

Figure 15: Potential suboptimal setup, with curling wires, moving the midpoint of discharge closest to the other electrode, which prevent the accurate measurement of electrode distance. Optimal setup is shown in Figure 13.

without complications, which is why the curling remains as an interfering factor and will be taken into account in the analysis by adjusting the distances between the electrodes. The setup uses two electrodes on opposite sides. As both electrodes have a curling tungsten wire at the tip, it is not straightforward to identify where the discharge takes place. A conservative perspective would state that the local electric field would be largest at the electrode tips and therefore the discharge would take place at the tips. However if the twisting of the wire is great enough, the discharge will change the ignition position. This is caused, as the local electric field is far greater at points closer to the other electrode. This can lead to heating at the points of greatest local electric fields, which may not be the tip. This results in thinning of the wire at the position of high temperature. With relatively large masses on both sides of this heating position, it becomes a possible point of fracture, where a break-off may occur. Figure 15 shows a possible setup for a possible fracture of the wire.

4.4 Plasma discharge in distilled water

The liquid used is distilled water and is stored in a big container at room temperature. Every time the chamber is filled with water, it is verified, that the temperature of the water is still at room temperature and the conductivity is measured. The chamber is filled with water, yet it is not fully filled, as to leave space for the liquid, as it may leak through the open valves. With the chamber filled with water, the electrodes already installed and two valves on the top side of the chamber opened, the ignition process is ready to start.

4.4.1 Ignition and initiation specifications

To initiate the discharge, the function generator and the high voltage generator are set to the desired parameters. Frequently used parameters would be 100 Hz and 10 % duty cycle for the function generator and 20 kV and around 2 mA for the high voltage generator. With the parameters set and the generators powered, the ignition will begin. As the discharges are occurring, the electrodes and the water starts heating and the temperatures of both rise. The electrodes are exposed to more heating, yet as the electrodes are fully submerged in the liquid, these temperatures start to equilibrate continuously. As this equilibration is not instantaneous certain parts of the liquid are heated faster. This leads to local vaporization of the water and consequently increasing the pressure of the chamber. Therefore, the valves are kept open for the pressure inside the chamber to equilibrate with the atmosphere outside the chamber. It also leads to large bubbles forming at the electrode.

4.5 Copper treatment with Plasma activated liquid

Treatment to the copper surface is applied shortly after treatment of liquid is finished. As reactive species, produced by the discharge, have an short life span, the treatment of the surface should take place promptly. The life time of pure hydrogen peroxide in an aqueous solution is a sensitive parameter. Its half time is in the range of a few hours to a few days, depending on temperature, pH, light irradiation, air humidity and many other parameters[25].

4.5.1 Treatment of copper surface

To effectively study the effects of the reactive species created during the discharge, the treated liquid is deposited on the sample. Small quantities of liquid will evaporate with an evaporation rate following the parameters of room temperature, air humidity and light irradiation, therefore energy input[26]. The process of evaporating the liquid on the sample is the most efficient and simple approach of adjoining hydrogen peroxide and the copper sample. The evaporation of the liquid droplet will cause its edge to evaporate first. As the droplet shrinks in size the water content will diminish and the reactive species will remain in the droplet. As the liquid droplet shrinks inward, the interaction area with the surface becomes smaller. This will reduce the reaction time the reactive species have with the outmost areas of the droplet. This causes the reactive species to accumulate in the center of the shrinking droplet, which increases the reactivity in that area. Therefore the placement, amount and storage of the treatment is important to document. The freshly treated liquid is applied to the recently coated copper sample. Using old samples or liquid can alter the results. A droplet of 40 µl is

applied to a sample and it will take about three to four hours for a droplet of this size to evaporate. Throughout the evaporation process, the sample is stored unconcealed in a room with either an open window or a ventilation system, to ensure the evaporation process takes place. Ensuring that the droplet evaporates correctly, a frequent check the sample is advised to minimize the time between the end of the treatment process and the start of the analyzing process.

4.6 Analyzing the copper surface using cyclic voltammetry

The last steps are to analyze the surface using cyclic voltammetry and later SEM. Cyclic voltammetry is delicate, as every change in the procedure can lead to different results. Therefore a detailed description is issued in the following section.
When the evaporation process is finished, the copper surface sample is taken to the cyclic voltammetry setup. Here, the sample is set onto the orifice with the treated copper facing the gap into the chamber. The sample is then fixed into place by a plate which itself is locked into the chamber with screws. Caution was mandatory, as tightening the screws may cause the sample to break. After the sample is fixed, the chamber is set into its place and the electrolyte is added. The lid is put onto the chamber top, and then the argon nozzle, the counter electrode, the reference electrode and the resistance measuring electrode are introduced into the electrolyte. All wires and electrodes are connected to a potentiostat, which is also connected to the computer. This ensures, that the electrodes are read correctly and the working electrode can be powered. The argon gas bottle and its corresponding valves are opened, the butterfly valve for precision control of the argon flow is adjusted and the controller and PC is turned on. With all things set up, the cyclic voltammetric process can start. To initiate the analysis the computer program "EC-Lab" is started and the program procedure is selected. A regular program starts with a delaying interval of about 30 minutes of recording the open circuit potential. This is to ensure that the argon bubbler can bind and therefore eliminate most of the free oxygen molecules from the electrolyte. This helps to distinguish the incoming signal, as almost no free oxygen atoms remain inside the electrolyte, one can be sure that the incoming signal is predominantly originating from the reducing oxygen species from the driven copper surface. After the delaying interval, the cyclic voltammetry starts and the potential of the copper electrode now proceed to the predetermined set potentials, being -0.4 V and -1.1 V. When the cyclic voltammetry ends, the program continues with a measurement to determine the resistance of the liquid. This measurement occurs shortly after the CV scan. This concludes all of the necessary steps to form a reliable assertion. Yet in this thesis some steps are repeated in order to analyze the procedure after the grown oxides have been reduced and therefore removed from the surface.

5 Results, analysis and discussion

5.1 Treatment of liquid

To further determine details of the experiment, conclusions are drawn to explain the recorded data. As the experiment uses 50 µm diameter electrodes, one can derive the electric field at the tip by the expression[9]:

$$E = \frac{2V}{r \cdot \ln(\frac{4d}{r})} \tag{8}$$

where E is the electric field strength, V is the applied voltage, r is the radius of the electrode and d is the distance between electrodes[9]. Using $V = 20\,\mathrm{kV}$, $r = \frac{d}{2} = 25 \cdot 10^{-6}\,\mathrm{m}$ and $d = 1\,\mathrm{cm}$, the electric field amounts to 2169 $\frac{\mathrm{kV}}{\mathrm{cm}}$. The dielectric strength of air and water vapor[6] is around 30 $\frac{\mathrm{kV}}{\mathrm{cm}}$ and the dielectric strength of distilled water was tested to be around 650 to 700 $\frac{\mathrm{kV}}{\mathrm{cm}}$[27]. This in turn means, that direct impact ionization of the liquid is possible, as the applied field exceeds the dielectric strength of distilled water. The electric field at the tip of the electrodes is large enough for local heating to occur. This entails the formation of temperature fluctuations in the water. If enough heat is generated, a bubble will form[9]. As the electric field strength decreases with increasing distance, only water in close vicinity of the electrodes is affected by dielectric breakdown.

5.2 Discussion of data

While the treatment of the liquid was taking place, a Rogowski coil and a high voltage probe was operated in parallel to the experiment, as shown in Figure 8. The current and the voltage were monitored with an oscilloscope and the corresponding graphs were documented. The hydrogen peroxide concentration was determined with absorption spectroscopy. It was measured with a non-automated optical absorption setup and also with an automated instrument built for absorption spectroscopy. In the following chapter the recorded data are discussed.

5.2.1 Frequency generator, voltage and current graph

The determination of parameters has an effect on the discharge, therefore the parameters have to be chosen with care. Choosing a voltage too low results in the ignition being too weak and choosing a voltage too high may result in the ignition heating the chamber too fast, which is impractical for longer treatment times, as parameters such as conductivity and bubble generation are influenced by heat. The parameters chosen represent the most advantageous ignition for a 60 minute treatment with significant hydrogen peroxide

production. The parameters chosen are 20 kV voltage, 100 Hz frequency of discharge, 50 µm electrode diameter, 1 cm electrode tip distance and 60 minute treatment time. These parameters are hence called standard parameters. Nevertheless, there are still parameters that are recorded before ignition which also impact the results, being the room temperature, temperature of the liquid and conductivity of the liquid. Figure 16 depicts a recording of the voltage and current of the discharge, as well as the voltage of the frequency generator. The frequency generator voltage and discharge graph of the

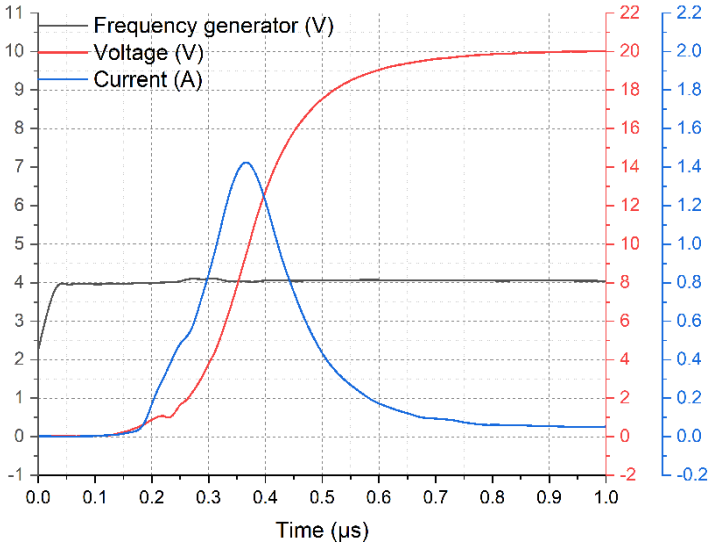

Figure 16: Graphs of the current and voltage curve of a single discharge and the frequency generator voltage.

voltage and current in Figure 16 was recorded with the standard parameters, after 10 minutes of treatment time. The frequency generator voltage shows the point in time, where the capacitor is triggered. Figure 16 shows, that after the initial trigger voltage of the function generator, the capacitor takes about 200 ns to apply the current and the voltage to the chamber. As the current and the voltage start rising, one can see that the current peak is fairly early and it also decreases as fast as it increases. The full-width half-maximum of the current peak takes about 146 ns and has a peak current of 1.7 A. As one can see, the voltage graph also has a fast rise and after reaching its peal, the voltage slope is very small. Therefore it descends relatively slow to its rise. It takes about 150 µs for the voltage to reach zero again. It has a peak voltage of 20 kV. As the current and the voltage have been recorded, one can establish the calculation of the dissipated power inside the chamber during a single discharge.

5.2.2 Power and energy graph

With the acquired power graph over a discharge one can work out the energy used for a single discharge. The formula for power calculation is the elementary equation 9.

$$P = U \cdot I \tag{9}$$

Where P refers to the absorbed power, U refers to the voltage applied and I refers to the current measured. As the energy is the power applied over time, $[P] = \frac{J}{s} = \frac{[E]}{[t]}$, one can integrate the power graph over the discharge and acquire the energy used:

$$P = \frac{dE}{dt} \rightarrow E = \int P dt \tag{10}$$

Where E refers to the energy dissipated in the chamber, calculated by integrating power consumption with respect to time. Figure 17 shows the graph of a possible curve of a discharge with the standard parameters, containing every meaningful measurable parameter, recorded after 10 minutes of treatment time and a discharge frequency of 100 Hz.
Figure 17 shows the frequency generator voltage, the applied electrode voltage, current measured across the chamber, power calculated from voltage and current, energy dissipated as well as the resistance over the course of a single discharge.

An important factor to mention is that the peaks of all parameters are fluctuating in height. This is because the function generator and high voltage generator do not yield identical pulses and do not operate without fluctuations. Therefore, a variance of about $\pm 5\%$ is considered a minor error and henceforth not discussed in detail. As the frequency generator administers a voltage to the capacitor, the capacitor will subsequently release its stored charge as a form of applied voltage to the electrodes. As the unloading is an electric signal, the transmission is not instant and a delay of applied frequency generator voltage to the capacitor and the discharge voltage to the electrodes occurs. As one can see in figure 17 the delay amounts to roughly 200 ns. This delay mainly occurs due to the wire lengths and wire resistances used to connect the internal setup as well as the connection to the oscilloscope used to record the data. Important to notice are the voltage and energy graph, as they do not immediately diminish, whereas the current and therefore power graph have a relatively short drop off. The resistance graph is steadily rising from 0 to 400 kΩ after 1 µs.

5.3 Recording of electrical parameters

In order to analyze the magnitude of the influence of single parameters on the discharge, a variation of multiple parameters has been analyzed.

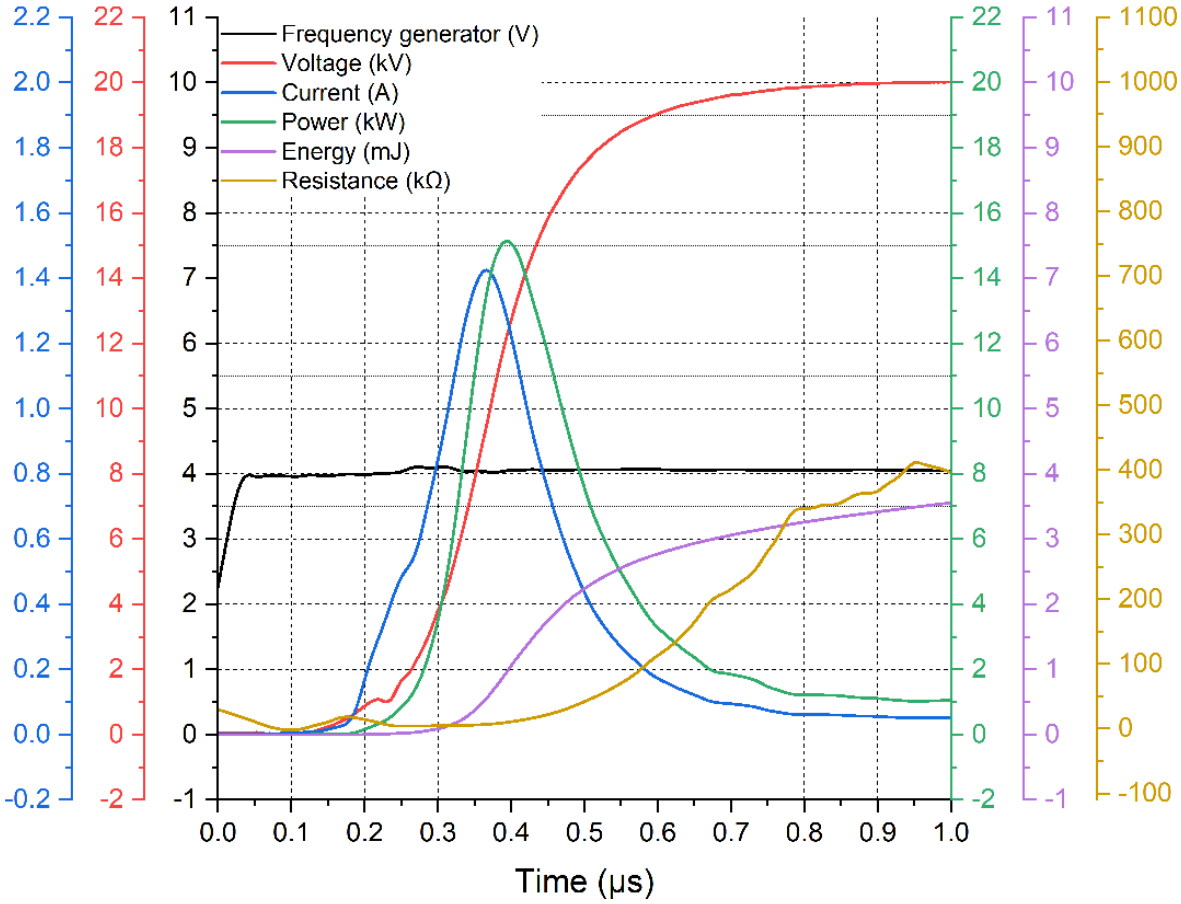

Figure 17: Measurement of applied frequency generator voltage, applied voltage to the electrodes, measured current and power, energy and resistance derived from the voltage and current, after 10 minutes treatment time.

The most trivial parameter variation would be the time variation. This variation will accompany all other variations, as the analysis of other parameters is based upon its time dependencies. Every parameter and graph changes with time, therefore the variation in every parameter will be illustrated. These measurement were performed multiple times and yield similar results.

5.3.1 Voltage variation as a function of time

The first investigation will be on the measured voltage. As the voltage is applied to the electrodes, its drop off will be measured across the chamber. Figure 18a and 18b are illustrations of the measured voltage across the chamber. Both illustrations originate from the same set of data. Noticeable are the time scales, as figure 18b has a large timescale of up to 200 µs and figure 18a only has a timescale of 1 µs. In other words 18a is a zoomed version of 18b, focusing on the start of the discharge. This is done to observe the behavior of the data at later times. There is a legend, linking the different colors of the graphs to time. This time indicates how long the treatment of water has been continuing at the time of recording. As one can see, the voltage graph resembles an

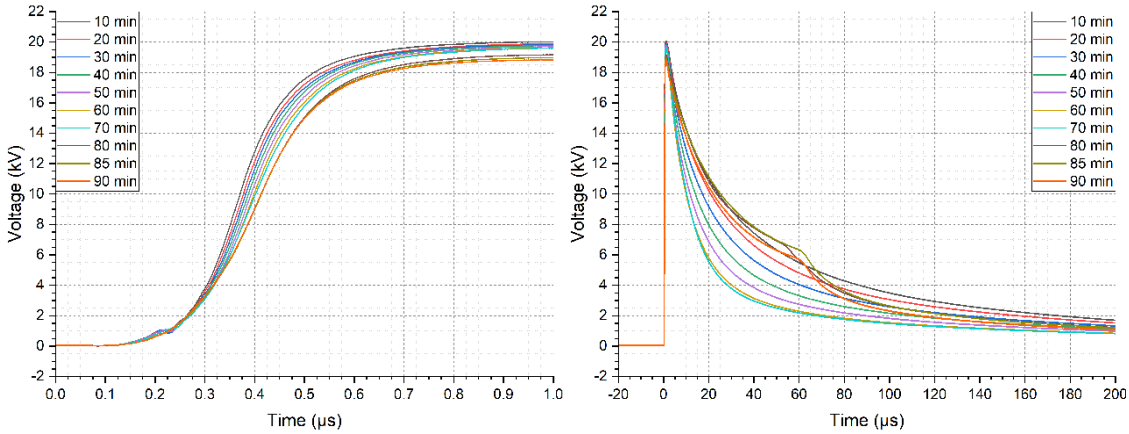

(a) Zoomed in version of voltage recordings across the chamber.

(b) Recording of voltage across the chamber.

Figure 18: Voltage recordings of water treatment at standard parameters.

exponential decay. At the start of the discharge all graphs are similar and no significant difference can be acknowledged. Yet, after 10 µs one can see, that the recorded graphs start to diverge. At minute 80 the graph changes its behavior, its decrease is not as fast and it also contains a bump. The change in behavior can be explained by a multitude of factors. For example, the heating of the electrodes has the effect that its material is dispersed in the liquid. This will increase the mean conductivity of the liquid and therefore benefit the number of discharges. This results in a self-amplifying effect, that can raise the number of discharges and therefore the amount of energy deposited into the water. This effect will be explained in detail in Section 5.4.
Having recorded the voltage graph, the next logical step is to measure the current, to calculate the power dissipated, energy dispersed and the resistance generated by the discharge. The next section will explain the recording of the current.

5.3.2 Current as a function of time

Figure 19 shows a depiction of current graphs with time dependence. Both illustrations depict the same graph but with different time and current scales. Figure 19a shows the current graph as the discharge begins and figure 19b shows the behavior of the current graph at long time scales. The rise time is 300 to 400 ns and the following decrease varies depending on the time. The decrease resembles an exponential decay. The graphs marked with 80-, 85- and 90 minutes have a noticeable distinction, as they do not fall off as quickly as the other graphs anymore. To note is that the graphs at 80-, 85- and 90 minutes display a negative power measurement, which would imply that some of the applied current is being returned.
This effect can most probably be explained by the fact, that the tungsten concentration in the water and the temperature of the water is increasing, the longer the treatment

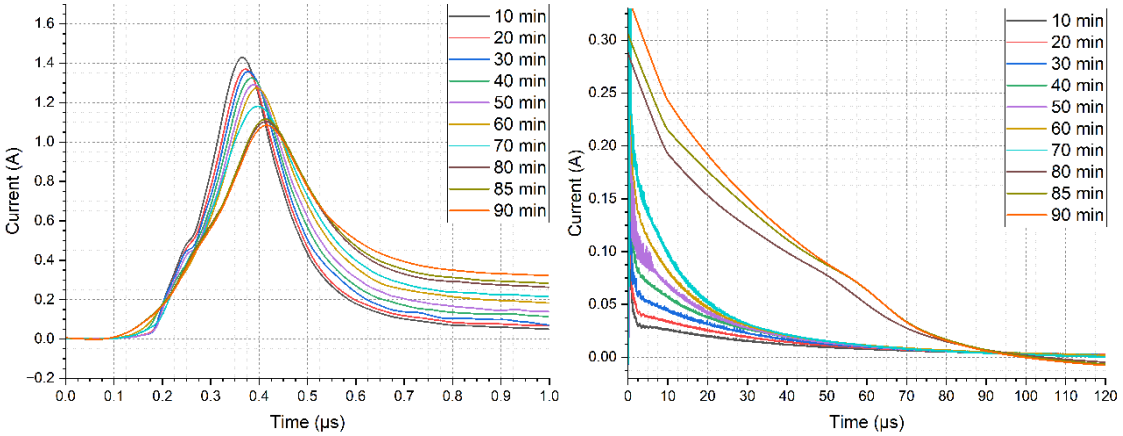

(a) Zoomed in version of current recordings. (b) Recording of current, obtained by the rogowski coil.

Figure 19: Current recordings measured using a rogowski coil, which was applied to the powered cable, measured at standard parameters.

is applied. Those factors benefits electric field propagation as well as increasing the ionization degree. This results in more charged particles that can be generated and therefore more gas channels can be generated. This entails, that more ions reach the electrode, which will generate a current, that opposes the applied current, which is recorded in the graphs of 80 to 90 minutes. The propagation of electric field and gas channels happen on a time scale of multiple microseconds[8]. The following plasma channels generating secondary streamers made from ions take up to a multiple of tens of microseconds[8], which explains the negative current in the graphs, observed at 90 µs in 19b.

Recording the voltage and the current allows us to calculate the power, energy and resistance, which will be done in the following chapters.

5.3.3 Power as a function of time

Figure 20 shows the power graphs recorded.

As power is calculated from the current and voltage graph with equation $P = U \cdot I$, the power graph resembles the current graph and the voltage graph. Since both graphs resemble exponential decay, so does the power graph. The time scales in 18a, 19a and 20a have been kept the same and the time scales in 18b, 19b and 20b are also the same. This has been done to enable a comparison between the different graphs. Since some of the current graphs become negative after 100 ns, so do some of the power graphs. This occurrence is not clearly visible, as the negative current is very small. The power graphs in the first microsecond after discharge are very similar. The height and drop off are changing with increasing treatment time. The peak gets increasingly delayed, from 390 ns after start of discharge to 450 ns after discharge. The slope also changes,

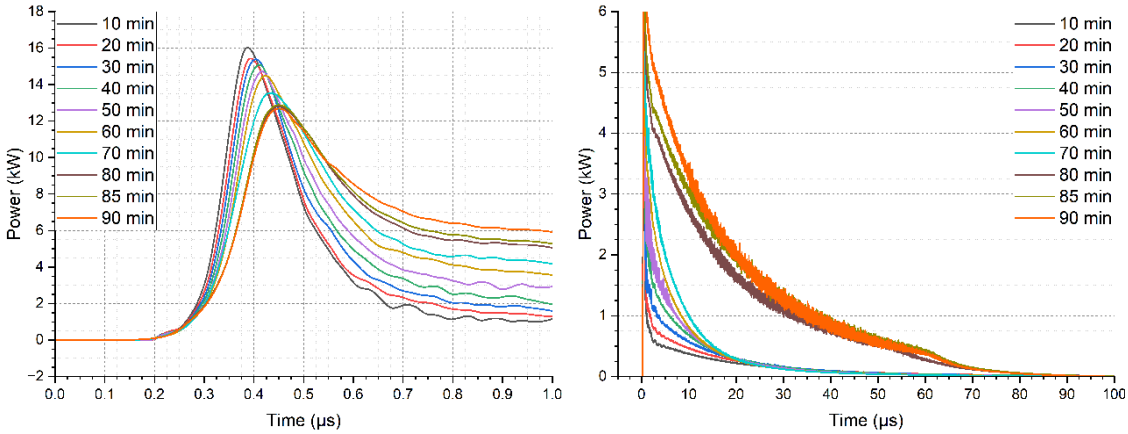

(a) Calculated power as a function of time.

(b) Zoomed out version of the power calculated, to observe delayed behavior.

Figure 20: Power graphs calculated using equation (9).

as at short treatment times the power drops to diminishing values after around 30 µs, where at longer treatment times it takes about 70 to 80 µs. Treatment times between 10 and 70 minutes have a steep slope, but the slope at 80 to 90 minutes is not as steep. This is mostly due to the effect of heating of the water, conductivity change at higher treatment times and water volume reduction. These changes benefit the number of gas channels forming within the discharge, which can explain why the power graphs at higher treatment times have a shallow slope.
Having calculated the power, one can conclude, that the mean power used per pulse increases with longer treatment times. At longer treatment times, the power graph shows a less steep slope than the other graphs. This is the same self-amplifying effect from the tungsten concentration in the water and the temperature of the water, which are also discussed in 5.3.1.

5.3.4 Energy as a function of time

Figure 21 shows an illustration of the dissipated energy dissipated within the discharge in reference to treatment time at standard parameters.

The graphs of 21a and 21b show the data of the calculated energy dissipated for a single pulse. Since the energy is calculated by integrating the power curve, the energy graph will have an asymptote, as the power curve approaches zero after the discharge. All graphs dissipate more energy the longer the treatment has been running. The energy graphs from minute 10 to 70 resemble a linear trend in that the difference between the height of the asymptotes roughly stays the same. Interesting to notice is a sudden difference from minute 70 to minute 80, where a large gap in the dissipated energy is observable. As the current becomes negative at around 100 µs, so does the power graph and consecutively the energy graph will decrease. the sudden jump in energy dissipated

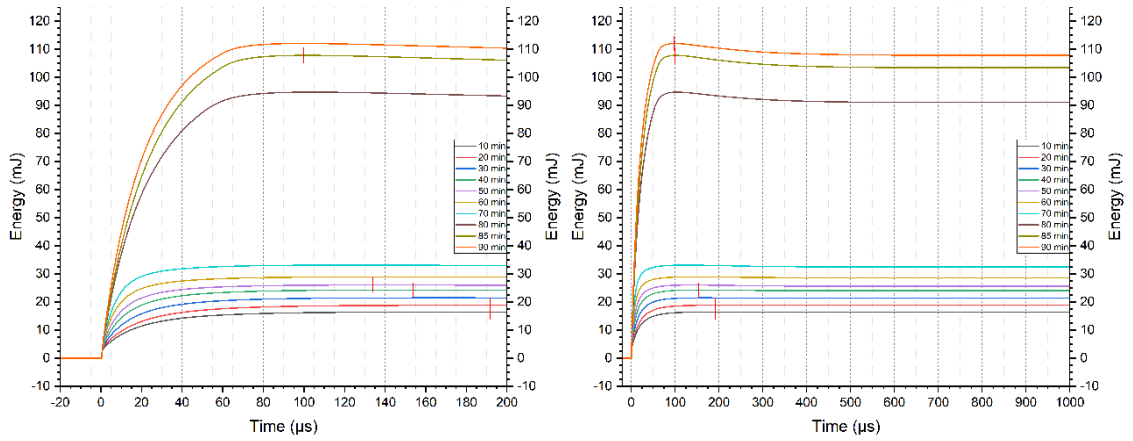

(a) Graph of energy of a single discharge

(b) Graph of energy of a single discharge with a larger time scale

Figure 21: Calculated graphs of dissipated energy of a single discharge, using equation (10).

can be explained by the mentioned temperature change and conductivity change of the water.

As a result of energy being dissipated in the liquid, local heating of the electrodes will occur. This in turn evaporates the surrounding liquid, forming a bubble and an atmosphere where plasma can be ignited. To form this bubble, the surrounding liquid has to receive enough energy from ohmic heating and evaporate. One can calculate the energy needed for a bubble with radius r to be formed. The energy required to heat the liquid $E_{heat.}$ and the energy required for evaporation $E_{vap.}$ are calculated separately.

$$E_{heat.} = m_l \cdot \Delta T \cdot c_h \tag{11}$$

$$E_{vap.} = m_l \cdot c_v \tag{12}$$

Where m_l is the mass of the liquid, ΔT is the temperature difference, c_h is the heat capacity of water with a value of $4180 \frac{\mathrm{J}}{\mathrm{kg \cdot K}}$ and c_v is the latent heat for water with a value of $2.26 \cdot 10^6 \frac{\mathrm{J}}{\mathrm{kg}}$[22]. As the liquid starts at room temperature 20 °C and evaporation starts at 100 °C, ΔT needs to be $\Delta T = 80\,\mathrm{K}$. The mass of the liquid can be transformed to be dependent on the radius r of the bubble[22]. Considering the difference in density of water vapor and water, one can see that for a bubble of vapor to form, a bubble of water with volume $\frac{V}{1700}$ must evaporate, as $\frac{V}{1700}$ is the converted water volume from vapor volume.

$$m_l = V_w \cdot \rho_w = \frac{V}{1700} \cdot \rho_w = \frac{4 \cdot \pi \cdot \rho_w}{3 \cdot 1700} \cdot r^3 \tag{13}$$

Where V is the volume of the bubble and ρ_w is the density of water with a value of $1000 \frac{\mathrm{kg}}{\mathrm{m}^3}$.

Furthermore one has to consider the potential energy stored in the surface tension of

the bubble, as well as the pressure equilibrium, as bubble and liquid have different pressures.
The potential energy stored in surface tension is calculated using equation (14).

$$\gamma = \frac{E_{surf.}}{\Delta A} \tag{14}$$

Where γ is the surface tension, $E_{surf.}$ is potential energy stored in surface tension and ΔA is total surface increase.
The surface tension γ of water at room temperature is $72\,\frac{\mathrm{mN}}{\mathrm{m}}$ and the total surface increase is dependent on the radius of the forming bubble. One can represent the change in surface area as $\Delta A = A_b - A_0 = 4 \cdot \pi \cdot (r^2 - r_0^2) = 4 \cdot \pi \cdot r^2$, with r_0 as the initial radius with $\mathrm{r}_0 \ll \mathrm{r}$.
One can rewrite $E_{surf.}$ as

$$E_{surf.} = \gamma \cdot 4 \cdot \pi \cdot r^2 \tag{15}$$

Now one can calculate the potential energy of the bubble with respect to the pressure difference, using equation (16).

$$E_{pres.} = V_b \cdot (p_w - p_v) = \frac{4}{3} \cdot \pi \cdot r^3 \cdot (p_w - p_v) \tag{16}$$

Where $E_{pres.}$ is the potential energy from pressure difference, V_b is the volume of the bubble, $p_w = 101325\,Pa = p_{atm}$ is pressure of surrounding liquid, p_v is pressure of vapor inside bubble and r is radius of bubble[22].
As electrodes are not far submerged from the surface, it is safe to assume, that the water surrounding the electrodes has atmospheric pressure.
Now, one can calculate the pressure of the vapor in the bubble.

$$p_h = \rho_w \cdot g \cdot h + p_0 \tag{17}$$

Where p_h is the pressure at depth h, $\rho_w = 1000\frac{\mathrm{kg}}{\mathrm{m}^3}$ is density of the liquid, $g = 9.81\frac{\mathrm{m}}{\mathrm{s}^2}$ is gravitational constant, p_0 is atmospheric pressure and h is depth. Calculating pressure at approximately 8 cm beneath the surface, we obtain $p_{8cm} = 102084\,\mathrm{Pa}$. Therefore the pressure 8 cm beneath the surface has 784 Pa more than atmospheric pressure, this amounts to an increase of 0.77%.

The total energy needed to form a bubble is obtained by adding the energy of evaporation, heating, potential energy of surface tension and potential energy of pressure difference.

$$E_{total} = E_{heat.} + E_{vap.} + E_{surf.} + E_{pres.} \tag{18}$$

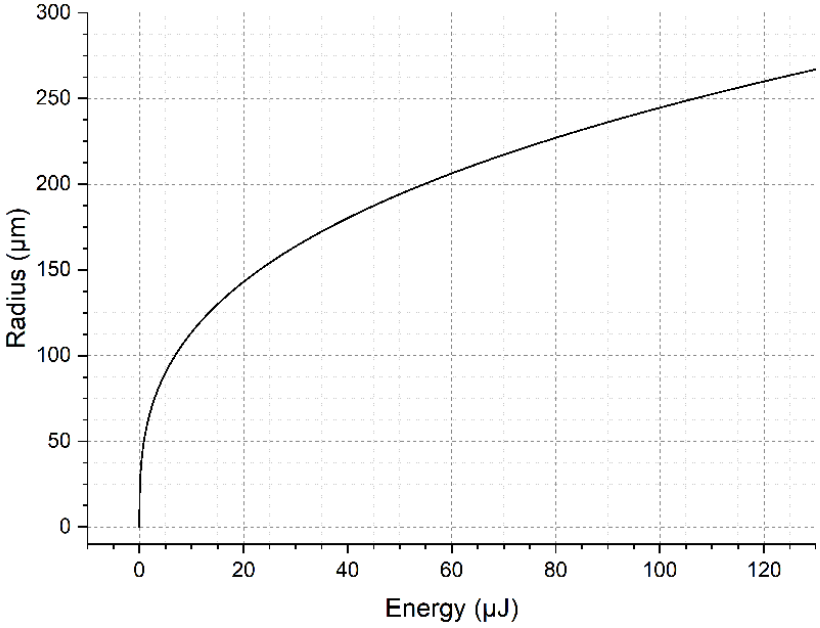

Figure 22: Bubble radius as a function of energy input, using equation (20).

$$E_{total} = \frac{4 \cdot \pi \cdot \rho_w}{3 \cdot 1700} \cdot r^3 \cdot \Delta T \cdot c_h + \frac{4 \cdot \pi \cdot \rho_w}{3 \cdot 1700} \cdot r^3 \cdot c_v + \gamma \cdot 4 \cdot \pi \cdot r^2 + \frac{4}{3} \cdot \pi \cdot r^3 \cdot (p_w - p_v) \quad (19)$$

$$E_{total} = \left(\left(\frac{4 \cdot \pi \cdot \rho_w}{3 \cdot 1700} \cdot (\Delta T \cdot c_h + c_v) + \frac{4}{3} \pi \cdot (p_w - p_v) \right) \cdot r + 4\gamma\pi \right) \cdot r^2 \quad (20)$$

With the radius r now only dependent on the dissipated energy E_{total}, one can estimate the bubble size with respect to energy input.

Figure 22 shows a graph of the energy dependency of the bubble generated. The recorded energy dissipated in the chamber is very large in comparison to the energy required to form a small bubble. As surface tension of bubbles inside water is inversely proportional to its radius, and pressure inside the bubble is also inversely proportional to its radius, it is highly likely, that mostly small bubbles are formed at the electrodes, as they are more stable than bigger bubbles. One can conclude, that bubbles are generated in multitude with each pulse at different treatment times. For example, a treatment time of 10 minutes results in 16 mJ of energy being dissipated each pulse, which generate many tiny bubbles with varying sizes. Referencing the highest dissipated energy per pulse at 90 minutes treatment time one achieves 108 mJ of energy.

An estimation can be formed by assuming all bubbles being the same size. In this context the uniform bubble radius is assumed to be 50 µm, because the electrode is 50 µm as well. As the bubble gets larger than the electrode diameter, it can not attach

as well to the electrode as if it were smaller, therefore it most likely will detach. The energy required to form a single bubble with radius 50 µm is 803.2 nJ. Assuming all energy is converted to heat and the generated heat does not flow into colder regions, one can assume that at 10 minutes treatment time $19.9{\cdot}10^3$ bubbles with a radius of 50 µm are generated by each pulse. Therefore, to form a large and visible bubble, e.g. $r = 0.5\,\text{mm}$, 10^3 bubbles with radius 50 µm are needed. This predicts a large bubble production of 20 large bubbles per pulse.
This does not fit the observed behavior of bubble production during measurement, as the production of larger visible bubbles is not as high as assumed. The observed large, e.g. $r = 5\,\text{mm}$, bubble production was close to zero at short treatment times and 1 bubble per 5 seconds at 60 minute treatment time. Therefore either not all energy is converted into heat or the heat is flowing into colder regions. The most likely explanation is that the heat flow is great enough to transport the energy into colder regions, therefore cooling hot regions, which slows down evaporation. This may explain why evaporation mainly occurs at later treatment times, where more energy is dissipated per pulse.

5.3.5 Resistance

Using the voltage graph 18 and the current graph 19 we can calculate the resistance using the elementary electrical equation (21):

$$U = R \cdot I \rightarrow R = \frac{U}{I} \tag{21}$$

Figure 23a shows the resistance graphs within the first microsecond of the discharge

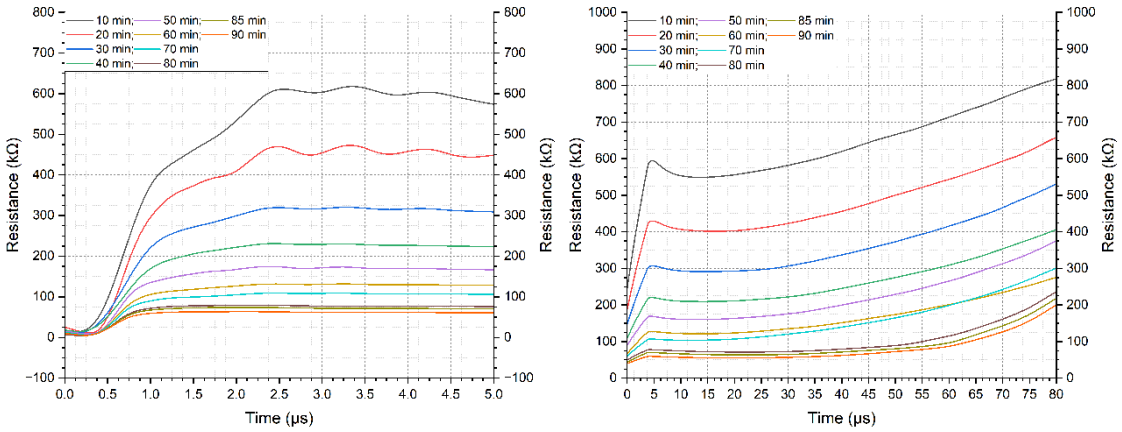

(a) Graph of resistance calculated at standard parameters.
(b) Graph of resistance with a larger time scale.

Figure 23: Resistance graph calculated at standard parameters in dependence of measurement time, using equation (21).

and figure 23b shows the resistances within the first 80 microseconds of discharge. One can see, that the resistance increases within the first few microseconds after ignition. Following the first microseconds of the discharge, the resistance graph slowly increases until 80 µs.
The time variation shows, that with increasing time the resistance per pulse steadily gets smaller. It first went from being around 600 kΩ at 10 minute treatment time to around 60 kΩ at 90 minute treatment time. This is most likely caused by material degradation and heating, which will be explained in Section 5.4. Knowing, that the resistance increases within the discharge and decreases with increasing treatment time, one can conclude, that the overall conductivity increases with treatment time. Furthermore, one can measure parameters of temperature, conductivity and hydrogen peroxide concentration.

5.4 Measuring and evaluating temperature, concentration and conductivity

Ex-situ conductivity and temperature measurements have been made, as these parameters hold information which help to further analyze the process of ignition in water. For example, the hydrogen peroxide generation rate may vary depending on the temperature of the water and the lifetime of H_2O_2 also depends on temperature of the medium[28]. The Temperature and conductivity were measured directly after the current and voltage are recorded. For this measurement, the water was transferred from the chamber into a small bottle, for easy transport and more easy access to the liquid. After the measurement of temperature and conductivity, the water is reintroduced into the chamber and the treatment of liquid can resume. The whole process of transferring the liquid, recording temperature and conductivity and reintroducing the water back into the chamber takes about 1 minute. Keeping this process short in time ensures that the measurement is as close to a continuous measurement as possible. The continuous change in parameters of the water can be explained by a self amplifying effect, which has an impact on many related parameters.
This self amplifying effect can be explained by multiple reasons. For example, electron avalanches induce ion currents, which can accumulate enough energy to dissolve the tungsten electrode. As tungsten is a metal, it can conduct currents and is more conductive than distilled water. Increasing concentration of tungsten particles in the water therefore increases the conductivity of the liquid. This in turn allows electron avalanches to further propagate into the liquid, increasing dissociation degree of the water vapor. It increases the number of available ions to form gas channels and increase energy accumulation. This is a self amplifying effect, the more energy is dissipated into the discharge, the more ionization is taking place, the more electrode material is

being dissolved and this again increases the energy dispersed into the discharge. These assumptions predict an exponential growth of temperature, conductivity and energy dissipated. This is due to the fact that when these parameters increase, it benefits further increasement. The following results may confirm this prediction.

5.4.1 Measuring temperature

Figure 24 shows the graphs of recorded temperatures for a 100 Hz discharge frequency and standard parameters. Important to notice in Figure 24 are the multiple mea-

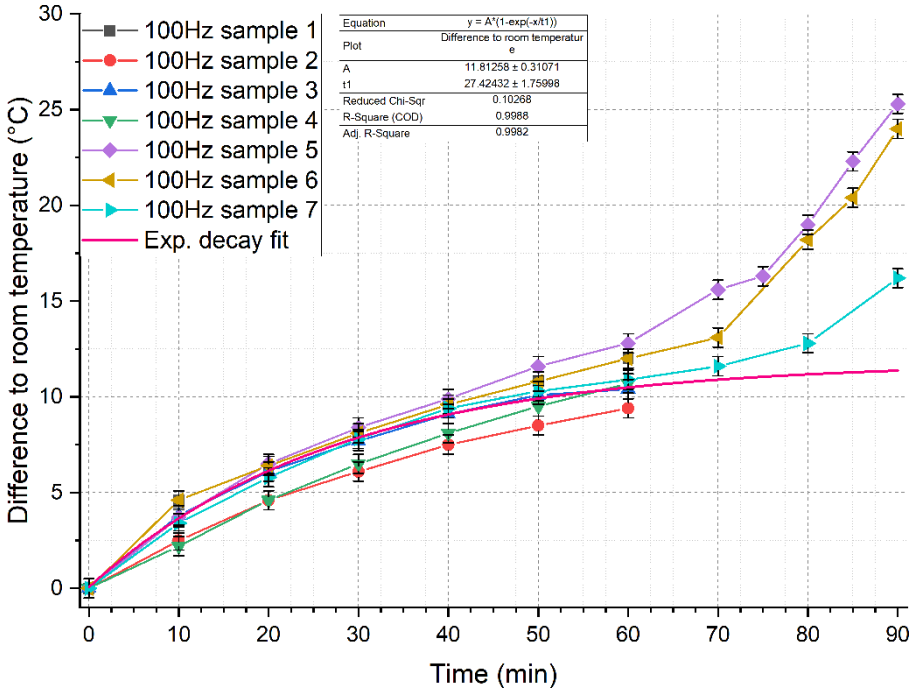

Figure 24: Multiple temperature recordings of water treated with standard parameters and an exponential decay fit.

surements done under similar conditions. Every different colored line represents a measurement done with similar circumstances, namely the same parameters. In the first 60 minutes, all of the graphs are similar to each other, resembling an exponential decay function. The starting temperature ranging from 17 °C to 21 °C, corresponding to room temperature. The curve of the temperature graph displays properties of an exponential decay function $A \cdot (1 - e^{-\frac{t}{B}})$, as its slope is decreasing, apparently leading to a horizontal asymptote. An exponential decay function fit was generated using the data and matches the behavior of the temperature data very well up to minute 60. Yet at longer treatment times the temperature is increasing much more rapidly again. At minute 70 to 80 the slope becomes larger than the slope at 0 minutes treatment time. A similar effect was observed by Mizuno et al.[29], where a comparable setup was used. The paper also drew conclusions on how temperatures are rising. They linked the

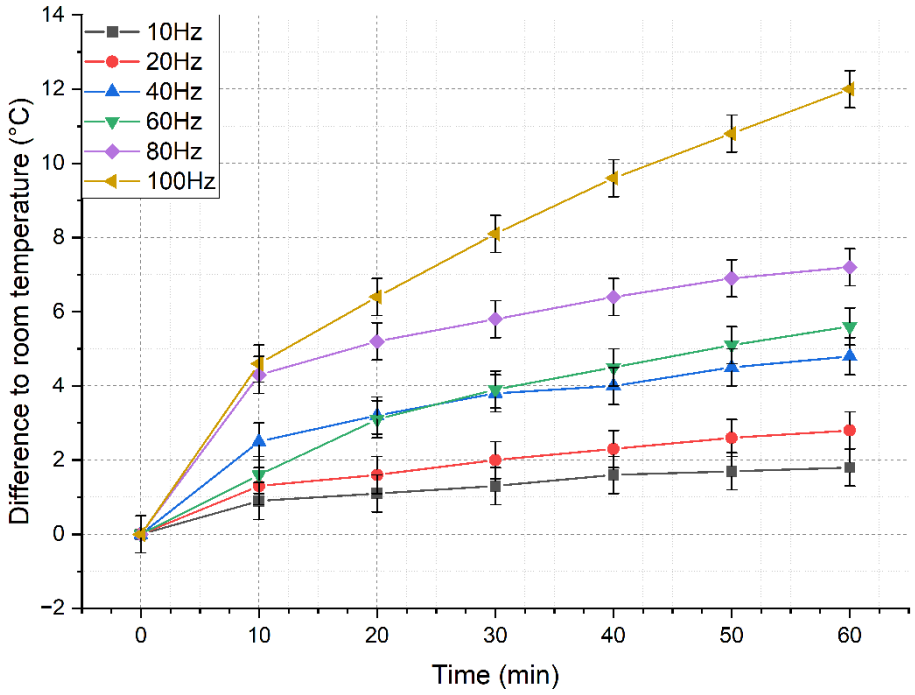

Figure 25: Temperature graphs using different discharge frequencies, using standard parameters.

evaporation and associated volume loss to the increase in temperature change[29]. If evaporation continues as normal, the volume of the water inside the chamber continues to decrease. This was also confirmed, as one experiment has shown. 30 ml of water was used for an experiment and after 90 minutes roughly 6 ml of water was evaporated. This is an effective reduction of 20 % of the total volume of water. The heat generated by the plasma has to spread over less volume, which leads to more heating within the remaining water. The heat capacity per volume has an inverse proportionality to the water volume. This indicates, that this effect of heat capacitance per volume unit increases significantly the smaller the remaining volume of water becomes. Yet such drastic changes in slope can not be explained only by a 20 % reduction of volume, which is why an other type of discharge is possible and why further research may be conducted.

Figure 25 shows the graph of recorded temperatures of water at different discharge frequencies. In Figure 25 one can see, that the temperatures of all used frequencies increase. The largest increase of temperature to 12 °C is observed at the greatest used frequency 100 Hz. The least increase to 2 °C is observed with the smallest used frequency 10 Hz. This observation fits the previous assumptions, that the energy dissipated is directly proportional to temperature increase. Knowing that the temperature measurements are in line with the previous assumptions about energy dissipation, one can analyze hydrogen peroxide production.

5.4.2 Measuring hydrogen peroxide concentration

The following section will detail the hydrogen peroxide concentration measured using an absorption spectroscopy setup and the reference to the automated commercial instrument.

Figure 26 shows the graph of recorded hydrogen peroxide concentration, using the manual absorption spectroscopy setup, with ammonium metavanadate (NH_4VO_3) as a binder for hydrogen peroxide.

In Figure 26, one can see 9 different graphs of recorded absorption spectroscopy

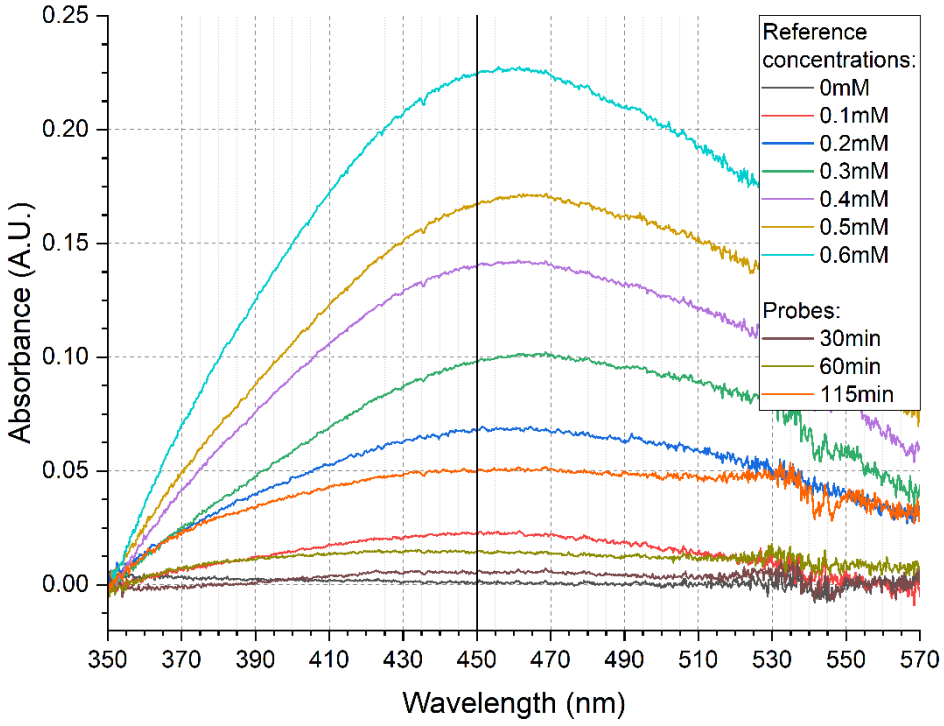

Figure 26: Absorption spectroscopy data, using 6 different known concentrations of hydrogen peroxide and 3 samples with different treatment times, at standard parameters.

data. 6 different known solutions are recorded to form a linear fit of concentration and absorbance. The 3 test samples have been treated with standard parameters, and collected at different treatment times, being 30 minutes, 60 minutes and 115 minutes. A line at x = 450 nm has been drawn to highlight the absorption wavelength of the hydrogen peroxide and ammonium metavanadate compound. As one can see, the concentrations of hydrogen peroxide in the test samples are all between 0 and 0.2 mM. Using the height of the graphs at 450 nm of the reference concentrations, one can construct a linear fit of concentration and absorbance. Figure 27 shows the linear fit constructed. In Figure 27 the 6 known concentrations are plotted and displayed using the black square sign. The 3 test samples are displayed using the red squares and the red line represents the linear fit, as displayed within the integrated legend of the graph.

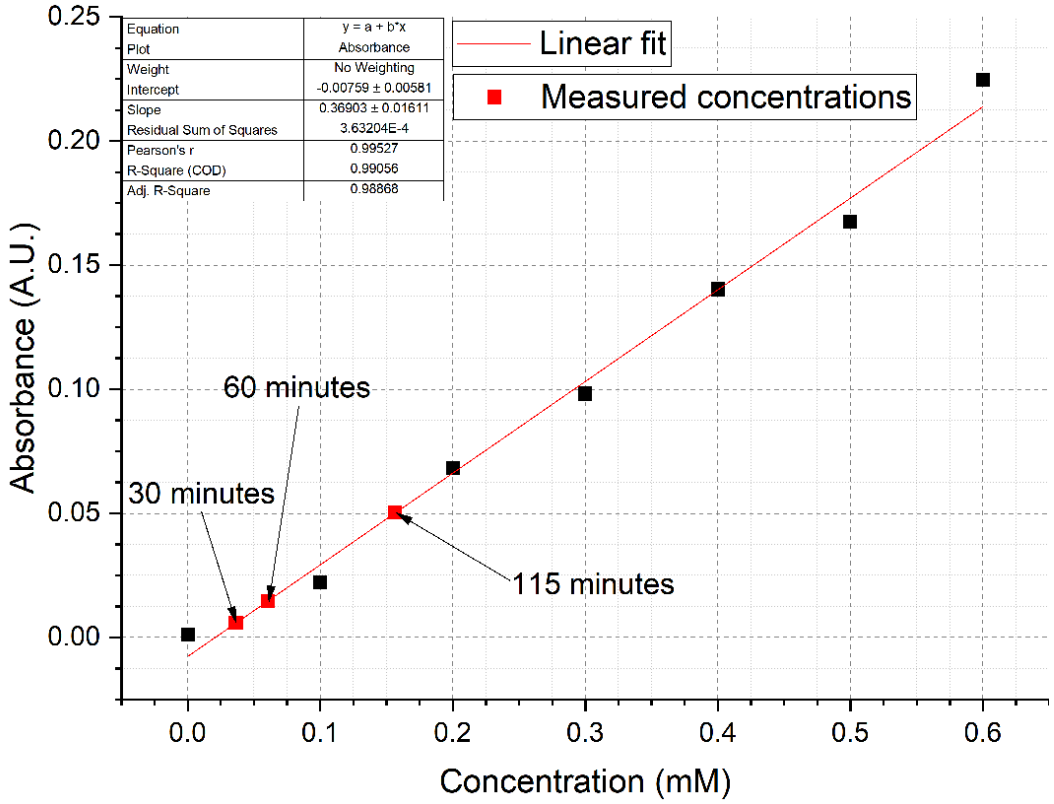

Figure 27: Linear fit of measured concentration with manual setup in dependence of absorbance, with test samples listed with 30 minutes at 0.036 mM, 60 minutes at 0.060 mM and 115 minutes at 0.156 mM concentration.

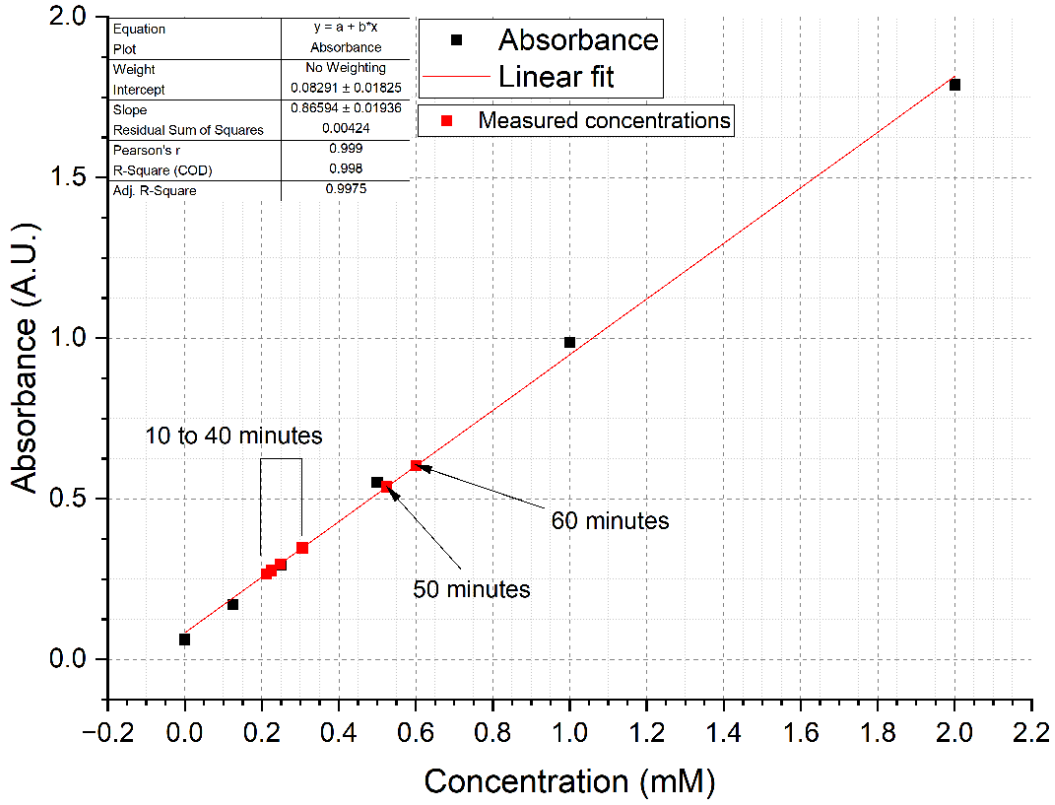

Figure 28: Absorbance graphs measured with automated setup with respect to concentration, 6 reference concentration used and 6 samples analyzed from 10 to 60 minute treatment time, treated with standard parameters.

An information text of the linear graph show the different parameters of the fit. It is a linear fit with the form $y = a + b \cdot x$ with $a = -0.00759 \pm 0.00581$ being the intercept and $b = 0.36903 \pm 0.01611$ being the slope. The residual sum of squares is close to zero and Pearson's r, R-Square (COD) and Adj. R-Square are close to one. This indicates, that the linear fit formed is very reliable on predicting results, as the discrepancy between observed data points and predicted data will be marginal. Using the form of $y = a + b \cdot x$ with the values for a and b, as well as using the measured absorbance of the 3 test samples, one can calculate the concentrations. The concentration for 30 minutes being 0.036 mM, for 60 minutes its 0.060 mM and for 115 minutes its 0.156 mM.

These concentrations will be compared with the concentrations measured with the automated absorption spectroscopy setup, which uses a binder for the hydrogen peroxide from a testing kit from Merck[30]. This testing kit provides a binder material compound, on which the mixture is not disclosed on their website[30], that if added to the hydrogen peroxide mixture also form a compound, of which the absorption wavelength is known to be 455 nm[30]. Figure 28 shows the absorption graph recorded with the automated setup. A linear fit was generated using the 6 known concentration and gave a fit of $y = 0.08291 + 0.86594 \cdot x$. The residual sum of squares, pearson's r, the R-square (COD) and the adj. R-square are all indicative, that the linear fit generated can

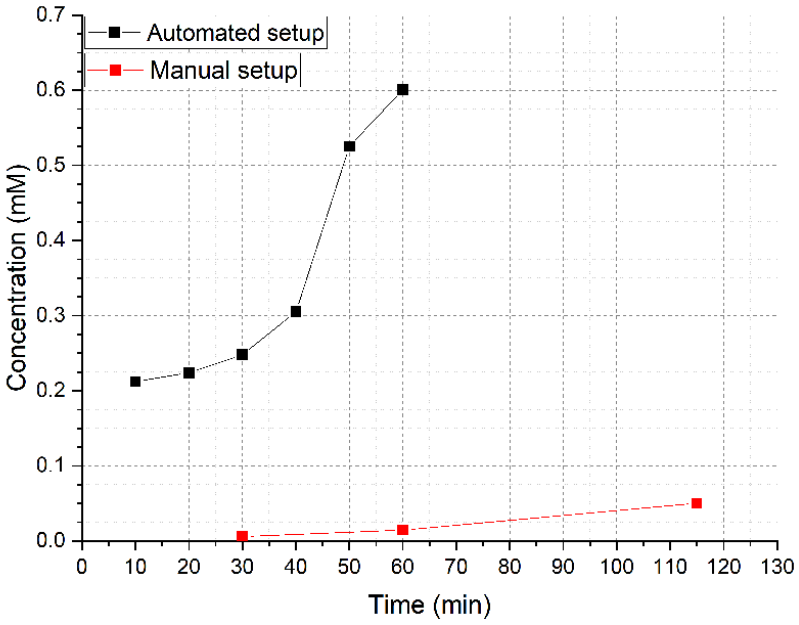

Figure 29: Concentration difference between the manual and the automated setup with respect to treatment time, using standard parameters.

accurately predict concentrations. With the fit, the concentrations of the different treatment times are calculated. 10 minutes at 0.21197 mM, 20 minutes at 0.22392 mM, 30 minutes at 0.24783 mM, 40 minutes at 0.30521 mM, 50 minutes at 0.52518 mM and 60 minutes at 0.60049 mM. This does not match with the concentrations measured with the manual setup. As the manual setup may contain impurities, such as light loss due to misalignment of lenses, dust particles and humidity in air, it can have inaccuracies and variance. These factors impact the automated setup to a much lesser degree, which is why the automated setup results will be taken as concentration measurement of this thesis. Figure 29 shows the graph of the comparison between the manual and the automated setup with respect to treatment time at standard parameters. Comparing the two graphs of concentrations achieved per treatment time shows, that the graph of the automated setup has a fitting curve for the fact, that the energy dissipated also has an increase.

Figure 30 shows the graph of the measured concentrations in dependency of used frequency for treatment at the automated setup at standard parameters. The change in concentration, which is dependent on frequency used, resembles a linear function, if the measurement at 80 Hz is regarded as inaccuracies. This is in good agreement with a paper from Chauvet et al.[31], where the topic of research is hydrogen peroxide production with nanosecond pulsed plasmas and the hydrogen peroxide production also increases linearly with frequency. As the frequency is directly dependent on the quantity of energy dissipated per second, one would suggest an exponential growth of concentration, as the self amplifying effects predict an exponential rise in temperature as

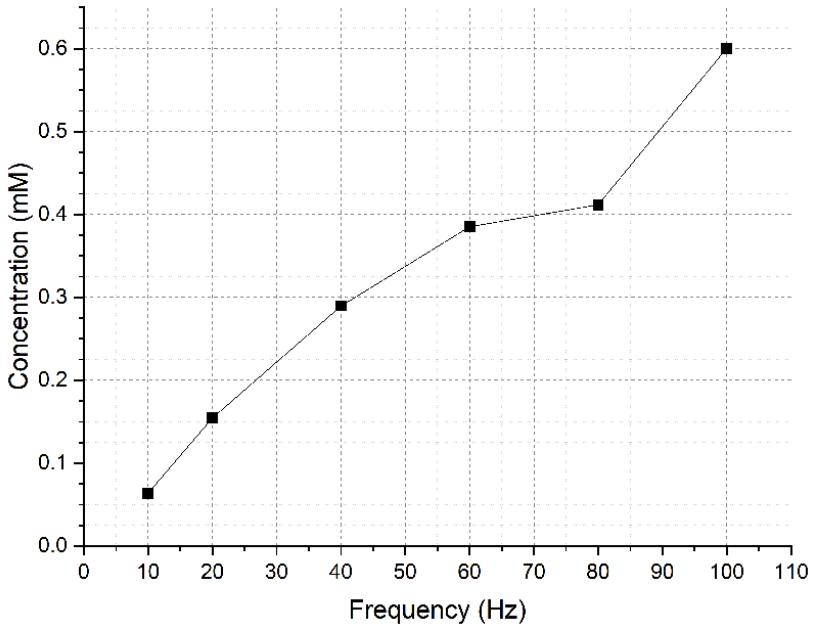

Figure 30: H_2O_2 concentration measurements in dependence of frequency used for treatment, measured at the automated setup and using standard parameters.

well. Papers from Gallo et al. and Ichikawa et al.[32][33] show, that hydrogen peroxide decomposition rate increases with increasing temperature. Higher decomposition rates in the vicinity of metallic surfaces are also attributed to surface catalytic effects, which are most likely due to a charge transfer process involving radicals[33]. As higher temperatures predict more energy dissipated within the water, more hydrogen peroxide will be generated. Yet at higher temperatures, the decomposition rates of hydrogen peroxide also rise. The rising decomposition counteracts the rising energy dissipation within the discharge. This would explain, why the concentration does not exponentially rise with frequency change.

5.4.3 Measuring conductivity

For the measurement of conductivity, a small sample of water was drained from the chamber and analyzed using a conductivity measuring device. Conductivity values measured from the samples are small in contrast to the measuring range of the device. This limits the measuring accuracy, as often times conductivity values between two whole numbers are present in the water, but the device can only display rounded numbers. Therefore an inaccuracy of $\approx \pm 0.5 \frac{\mu S}{cm}$ is estimated. Figure 31 shows the measured conductivity as a function of treatment time using standard parameters. As 7 different conductivity measurements were conducted using the same parameters, one can assume, that the conductivity graphs should be similar to one another. In Figure 31, one can see, that every measurement is indeed very similar, with a few outliers. The conductivity linearly rises from 1 $\frac{\mu S}{cm}$ to approximately 7 $\frac{\mu S}{cm}$ at 60 minutes. The 1 $\frac{\mu S}{cm}$ is

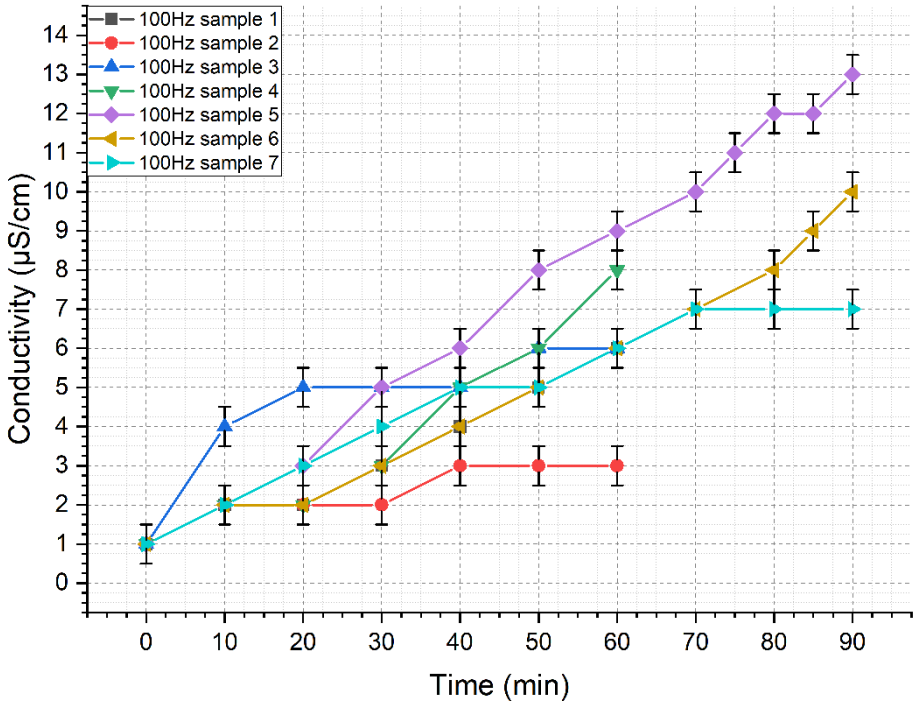

Figure 31: Multiple conductivity measurements using standard parameters at 100 Hz, with respect to treatment time.

the starting conductivity of distilled water used for treatment.
Figure 32 shows the conductivity measured at 60 minutes treatment time with varying frequencies. The graphs of Figure 32 do not yield curves with large differences, as many of the conductivities measured are close to the initial conductivity, as the lower frequencies used do not dissipate much energy. In fact, many of the lower frequency measurements share the same development, as the conductivity does not change much at all, sometimes only increasing by 1 $\frac{\mu S}{cm}$. From this one may conclude, that the electrode decomposition, which assumably causes the conductivity increase, gets increasingly weaker the less energy is dissipated within the system.

Having analyzed the electrical and external parameters of the discharge, one can explain the changes in dependence of one another and their potential effect on the cyclic voltammetry. Following section will detail the analysis of the cyclic voltammetric data.

5.5 Cyclic voltammetry

The settings of the cyclic voltammetry are chosen to start at a potential, where no reactions at the surface can take place. 0 V would be an ideal start. The potential is then cycling to -1.1 V, returning to -0.4 V and ending back at -1.2 V. This potential region was selected, because the reduction of copper oxides are within this region. Therefore a sweep over this potential range ensures, that all different reactions of copper are analyzed. The measured current starts at a voltage of -0.4 V and keeps changing,

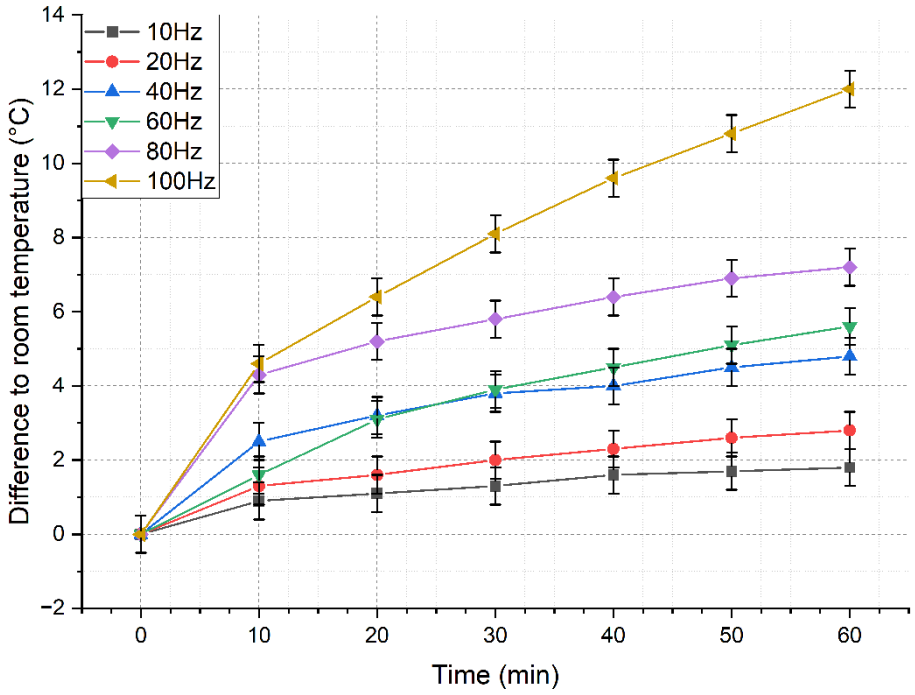

Figure 32: Conductivities measured in 60 minutes treatment time in dependence of the frequency used, at standard parameters.

until the voltage reaches -1.2 V.

Figure 33 shows the graph of cyclic voltammetry graphs using water treated with different frequencies. In Figure 33 the first overlay column represents the voltage region, where the crystalline copper (I) oxide is reduced, the second column represents the reduction region of an intermediate Cu_2O, the third column shows the region where amorphous copper (I) oxide is reduced and the last region is where CuO is reduced to Cu_2[16]. A blank copper surface and a copper surface treated with distilled water are added as a reference. One can see, that the difference between a blank surface and the surface treated with distilled water is not significant. Both have show a majority of intermediate copper oxides on its surfaces, with small amounts of amorphous cooper oxide. For reference, the surfaces treated with PAW have a considerable larger amount of crystalline copper oxides. The measured current peak of the graphs increases with increasing frequency. This is due to the fact, that the frequency is linked to the hydrogen peroxide concentration generated and therefore the oxidizing capability of the water. An increase in oxidation can generate more intermediate and crystalline copper oxides on the surface.

Figure 34 shows cyclic voltammetry graphs of copper surfaces, which are treated with distilled water with standard parameters. As shown in Figure 34, the process of analyzing surfaces using cyclic voltammetry is a delicate process. All graphs listed are cyclic voltammetric recordings of surfaces, which have been treated without any difference in parameter or procedure. Nonetheless, the graphs presents still a variation

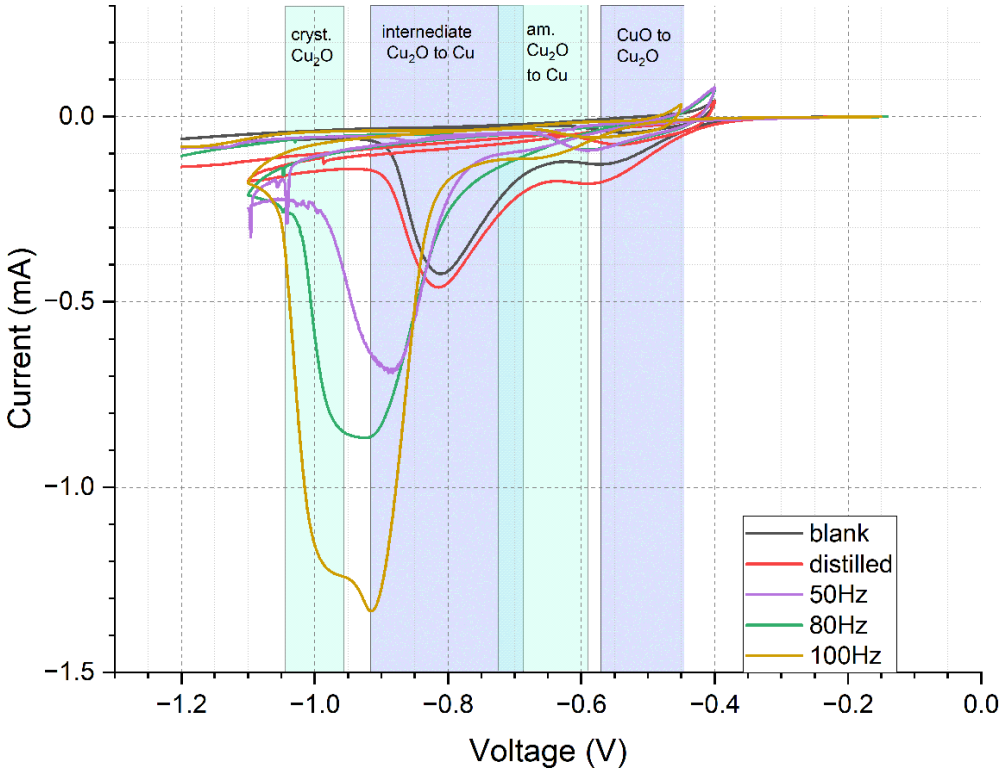

Figure 33: Cyclic voltammetry graphs of a blank surface, a surface treated with distilled water and surfaces treated with PAW with different frequencies, PAW treated surfaces recorded by Nils Huber.

of values of measured currents. Small difference in previously assumed unnoteworthy parameters such as evaporation time, humidity of air in the vicinity of evaporation and light irradiation during evaporation are estimated to cause a difference in the results, as they impact the speed of evaporation and therefore the time of interaction of water and surface. The process of recording a cyclic voltammetric graph also has potential sources of error, such as a bubble forming on the surface through the argon bubbler or any electrolyte residue.

Figure 35 shows a cyclic voltammetry graph recorded of a copper surface using water with 50 Hz and 30 minutes treatment time. The reduction cycle presents 3 peaks of current which all lie in different voltage regions where the different copper oxides are reduced. The first peak is in the CuO region, the second peak is in the intermediate copper oxide region and the third peak is in the crystalline copper oxide region. As the signal in the amorphous region are prominent, it can be assumed, that also a significant amount of amorphous copper oxide is present on the surface. As one can see, the graph at 50 Hz at 30 minutes is significantly smaller than the graphs with standard parameters. This is likely due to the longer treatment times and hydrogen peroxide concentration. Knowing the surface coverages of the different copper oxides, one can evaluate the electron microscope images in the next section.

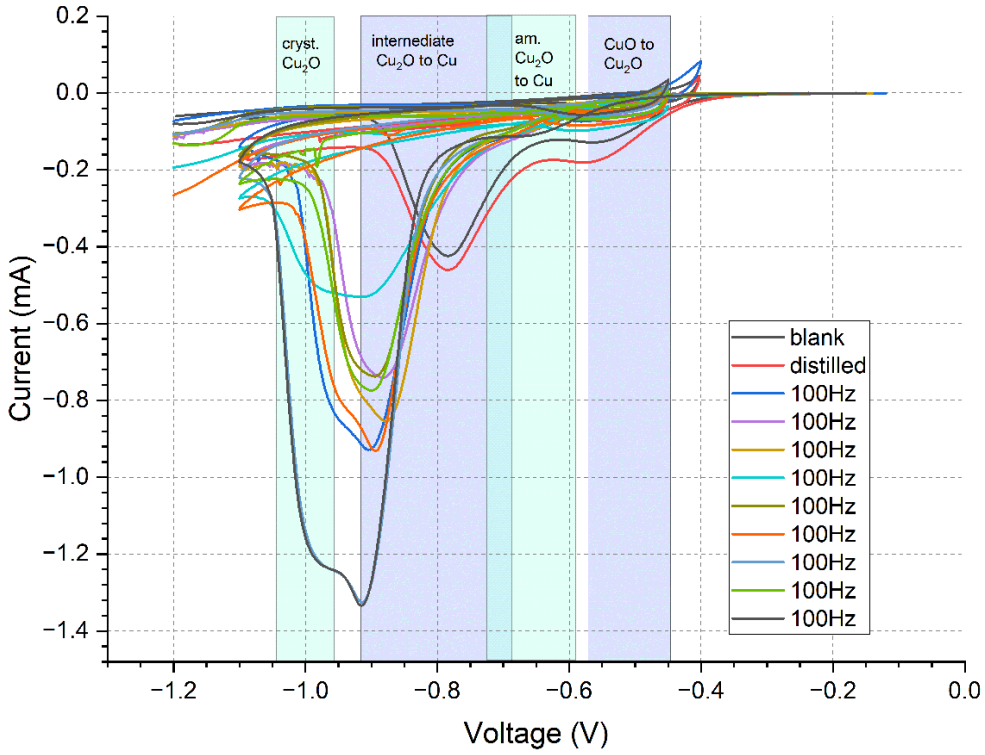

Figure 34: Cyclic voltammetric graphs of blank surface, surface treated with distilled water and surfaced treated with PAW at 100 Hz and standard parameters. PAW treated surfaces recorded by Nils Huber.

5.6 Scanning Electron Microscope results

The scanning electron microscope is a great tool for visualization of the copper surfaces. When copper crystals start to form on the surface, they are visible by SEM[34][35]. Copper crystals can form in a variety of different ways in the atomic lattice, with different orientations and different optical structures[35]. Figure 36 shows some of the most prominent possible orientations of the copper oxide crystal, when forming on the copper surface.

In this thesis the structure of the copper oxide crystals is polycrystalline and the orientation of the crystals is at random. The orientation can help to identify the different objects found on the copper surface with the SEM. As very low concentrations of hydrogen peroxide used on copper surfaces yield very little copper oxide crystals produced, it is difficult to identify the crystals. A copper oxide crystal almost always will maintain its form and its orientation, therefore they are more easy to verify.

Figure 37 shows a SEM image of copper oxide crystals on a copper surface using a SEM, found on a copper surface treated with PAW at standard parameters. In Figure 37 one can observe multiple copper oxide crystals. They are represented by the lighter color. The crystals vary in form and size and they gather around a large particle, which is several times the sizes of the single crystals. Some crystals have a clear orientation,

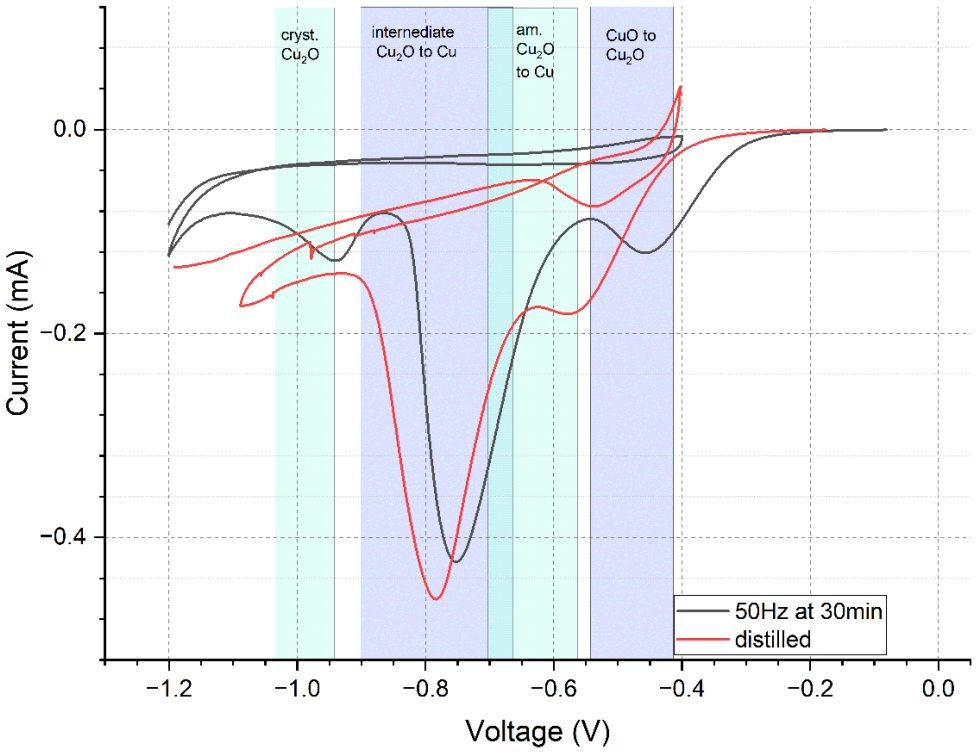

Figure 35: Cyclic voltammetric graph of surface with distributed coverage of copper oxides, surface treated with PAW at 50 Hz and 30 minutes and a surface treated with distilled water for reference.

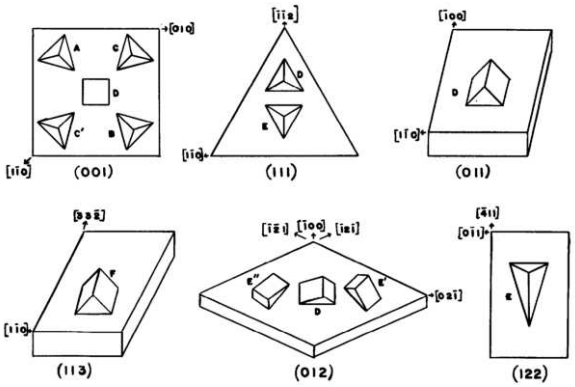

Figure 36: Most prominent oxide crystal orientations when forming on a copper surface, from [35].

while other crystals have many facets and do not have a clear orientation. Most of the crystals have a size of 100 nm and some of crystals are as large as 1 or 2 µm. Outside of the dense cluster of crystals is a gray area, where very small dots can be spotted. These are believed to be very small crystals, which are still forming. Crystals can form on the surface of other crystals, this causes some of the crystal to be within one another, and therefore display multiple orientations. This surface has been altered using plasma water treated with standard parameters. The droplet of plasma water has been placed on top of the copper surface and left to evaporate over 3 hours. The vast majority of a

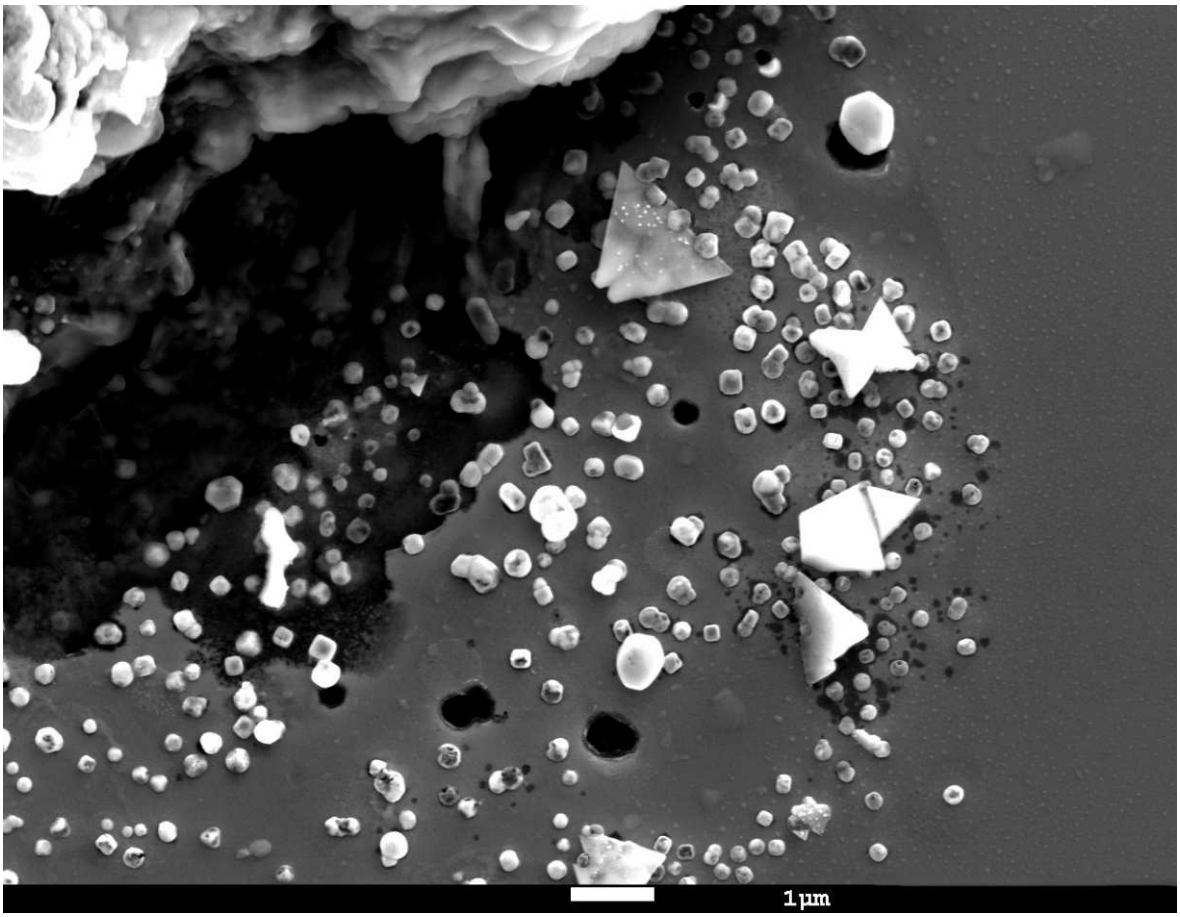

Figure 37: Cluster of copper oxide crystals on a copper surface with various orientations and formations, using PAW with standard parameters and drop evaporation time of 3 hours.

copper surface treated with PAW contains no visible particles.

Figure 38 shows two pictures of copper oxide crystals, where the oxide crystal clusters are recognized in the vicinity of other particles. Figure 39 shows pictures of oxide crystals formed evenly distributed on the copper surface. The pictures of Figure 39 show an evenly spread of oxide crystals forming and a single oxide crystal from the same surface. The surface was treated with standard parameters. In picture 39a one can see, that the oxide crystals all have sizes around 100 nm. In addition, one can see many impurities and dust particles.

Having observed local and evenly distributed copper oxide crystal growth, one can introduce a reference image of a surface treated with known concentrations of hydrogen peroxide. The concentrations used to form the reference images are many times the concentrations generated by plasma. This provides a broad simplification of what might be expected. Figure 40 shows pictures of a copper surface treated with different concentrations of hydrogen peroxide. The first two pictures 40a and 40b in Figure 40 are copper surfaces treated with a 1 M hydrogen peroxide concentration. Figure 40a shows a broad picture of the surface, as it is far more bright, than surfaces treated with

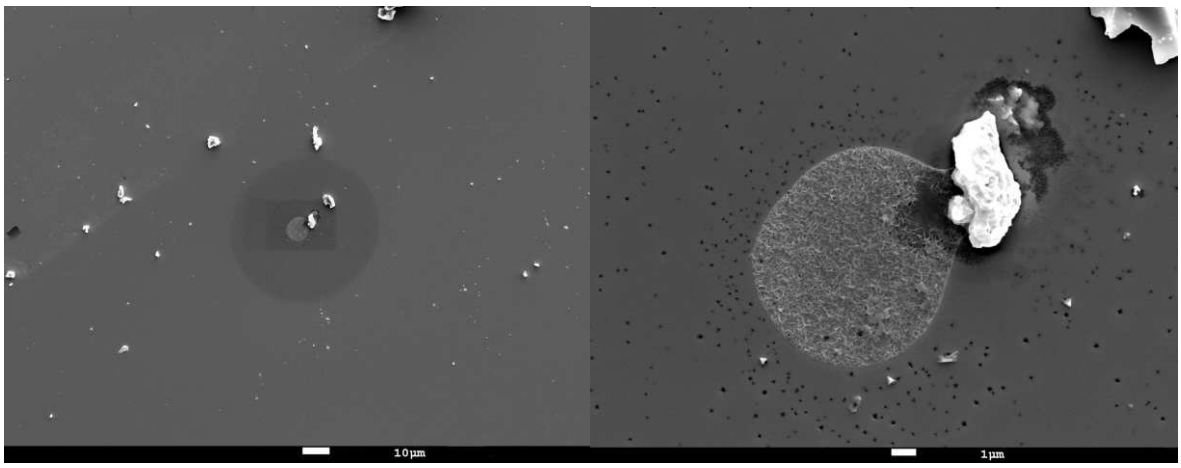

(a) Vastly empty copper surface treated with PAW(b) Zoomed in version of 38a. Large particle with Some dust particles are visible as bright objects on the surface. Crystal cluster formation around dust particle.

adjacent cluster of copper oxide crystals and single crystals forming near the cluster.

Figure 38: Copper oxide crystal formation along particles

plasma activated water. This is due to significant crystal growth. Crystals grow evenly along the surface and form a large cluster. In Figure 40b one can see the details of the large crystal cluster. It consists of many small crystals. The last pictures 40c and 40d show a copper surface treated with a 30% concentration solution of hydrogen peroxide which can be translated to a 16.6 M solution. Figure 40c has a comparable size scale as Figure 40b. The comparison between 40b and 40c shows, that the oxide crystals in 40c are much smaller than the crystals in 40b. This is due to the high concentration used, as higher concentrations entail a higher oxidation rate and therefore the oxide crystal generation rate is increased as well. This leads to dendritic crystal structure generated on the surface, with a size much smaller than the surface treated with lesser concentrated solution. Picture 40d shows the edge of the treatment. It is where the initial water droplet was applied to treat the surface. Interesting to note is the oxide crystal growth lessening at the edges of the water drop. There is an area between the crystal cluster and the clean copper surface, where only a few crystals started forming. The SEM images have shown, that the hydrogen peroxide has caused copper oxide crystal growth on the surface, which is indicative of the oxidization of the surface. Higher concentrations have shown, that the crystal growth rate is proportional to the hydrogen peroxide concentration used to treat the surface.

To conclude the SEM images one can say, that the desired result was achieved, that the copper oxide crystals are forming and are visible by SEM. The crystals formed using PAW are few but have a clear structure. The reference concentrations of H_2O_2 created many crystals, leading to a cluster of crystals with undefined structure.

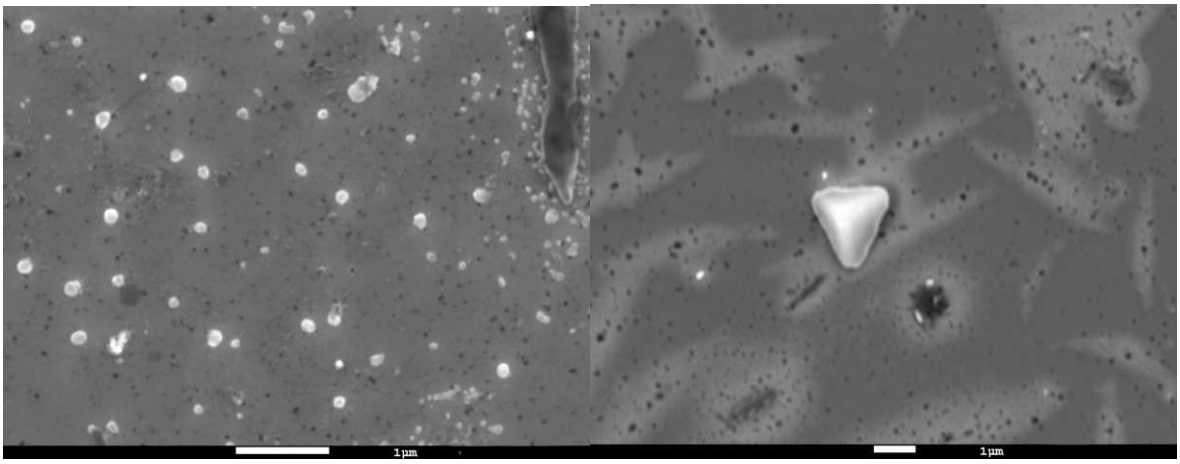

(a) Area of high oxide crystal density. Most of white objects are assumed to be oxide crystals.

(b) Single crystal found on the same surface as 39a.

Figure 39: Example of anisotropic oxide crystal growth on a copper surface treated with PAW at standard parameters.

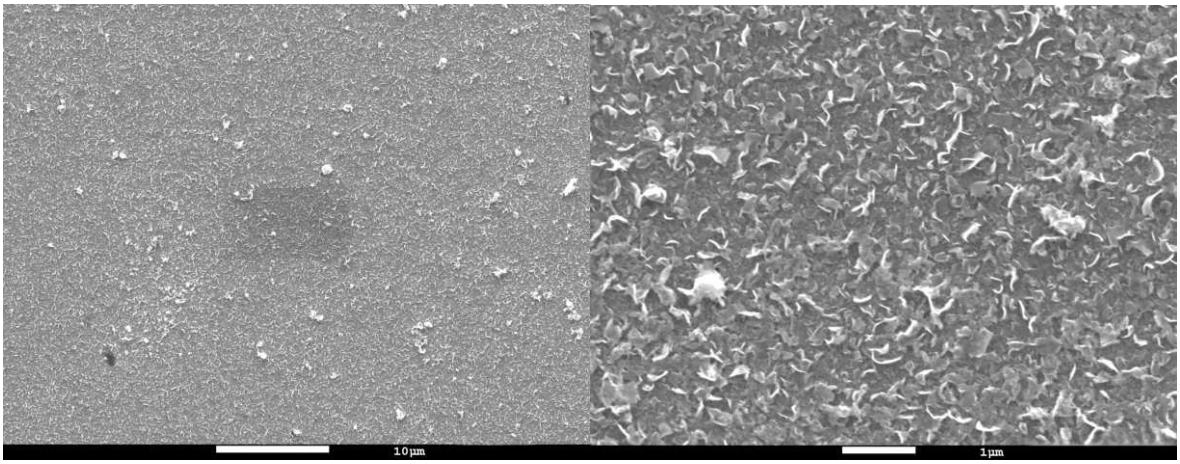

(a) Surface treated with 1 M hydrogen peroxide.

(b) Zoom of 40a.

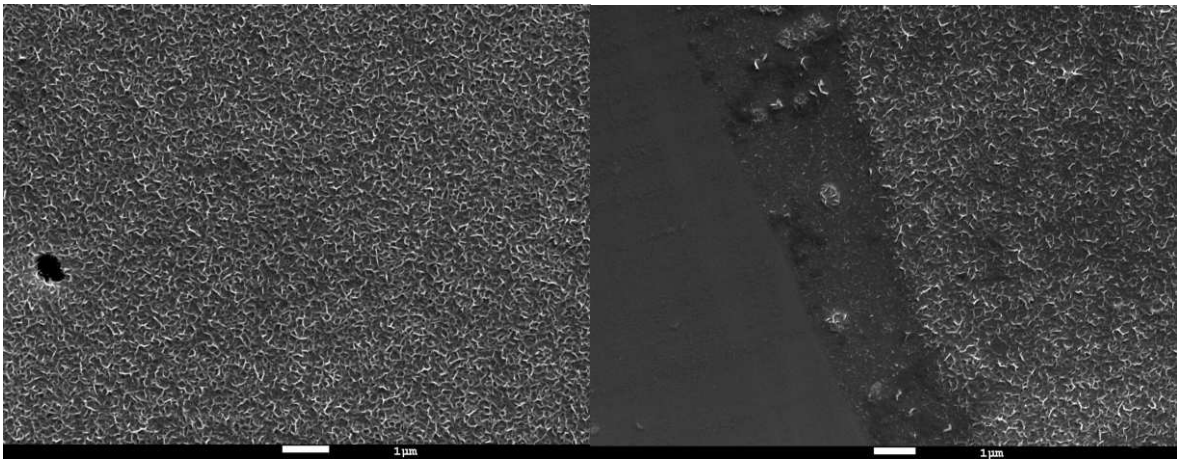

(c) Surface treated with 16.6 M hydrogen peroxide.

(d) Edge of 16.6 M treated surface.

Figure 40: Surfaces treated with different reference concentrations of hydrogen peroxide.

6 Conclusion

In conclusion one can say, that the analysis of the hydrogen peroxide generation in microsecond pulsed plasmas and the subsequent analysis of reoxidation of copper surfaces using cyclic voltammetry was successful, as the concluded data matches with literature[16][35][12]. The most remarkable occurrence is the sudden acceleration of heat generation and the subsequent sudden increase in energy dissipation per pulse. The most plausible explanations for this phenomena is the parallel increase in tungsten and volatile species concentration in the water and the water volume loss due to evaporation. Figure 41 shows the comparison between temperature, conductivity and energy dissipation per pulse. As one can see, the temperature graph increases steadily

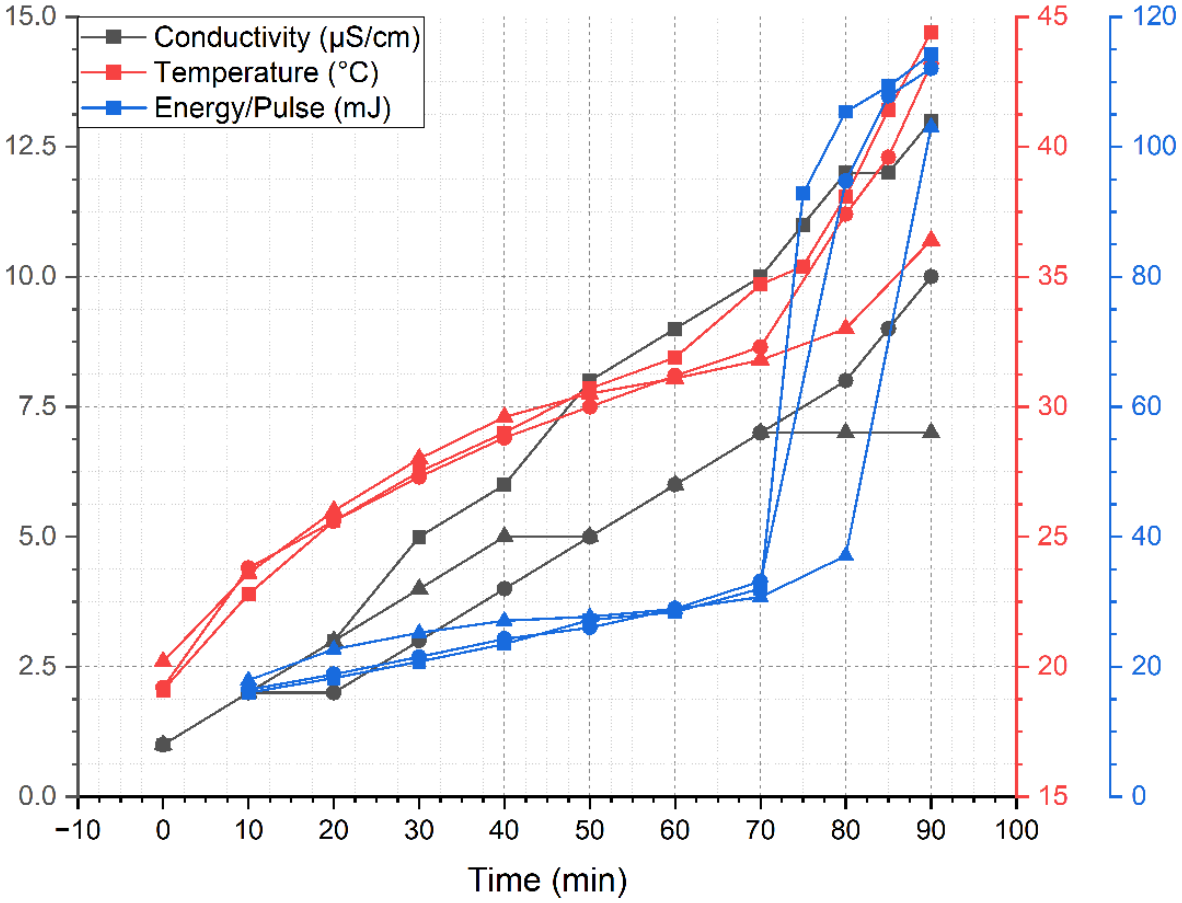

Figure 41: Comparison between temperature, conductivity and energy graphs, at standard parameters.

until minute 70, where it increases significantly. The energy per pulse also increases consistently, until again at minute 70 the graph increases significantly. In contrast to the temperature graph, the energy graph does not continue to increase significantly, as the slope gets smaller after the increment at minute 70. The interesting thing to note is that the conductivity only increases linearly. It was assumed, that the conductivity is proportional to the energy dissipated per pulse, yet Figure 41 shows, that when the

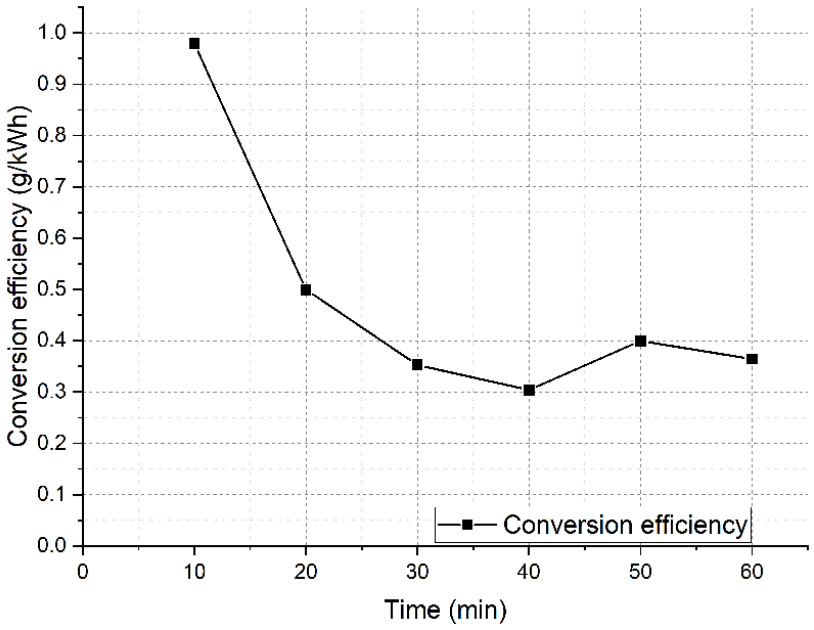

Figure 42: Hydrogen peroxide conversion efficiency, using standard parameters.

energy per pulse has an increase, the conductivity does not increase as much. This supposes, that the conductivity is not directly proportional to energy dissipated.
An attractive parameter which has not yet been discussed is the hydrogen peroxide conversion efficiency, which is shown in Figure 42. The efficiency is calculated using the energy dissipated per pulse, quantity of pulses and the concentration increase at given times. This result is in good agreement with other studies[28], for example, the nanosecond pulsed plasma generation efficiency give values of up to $2\frac{\mathrm{g}}{\mathrm{kWh}}$ at 5 minutes treatment time and otherwise standard parameters recorded by Chauvet et al.[31]. In the case of microsecond pulsed plasma discharges, the efficiency of converting water to hydrogen peroxide decrease steadily with increasing treatment time. This might be due to the effect of the increase in temperature as well as the increase in energy dissipated per pulse, where as the concentration increase does not increase as fast. An increase in temperature may cause hydrogen peroxide to degenerate more quickly[33].
The efficiency of microsecond pulsed plasmas is below the nanosecond pulsed plasmas in terms of efficiency. This might be due to the fact, that when the threshold of energy to form a plasma is reached, a plasma channel in the water vapor will form and adding a surplus of energy will not increase the amount of plasma channels created as much as expected. The excess energy will most likely heat the already heated water in order to counter act the heat flow to colder regions. This may be an explanation on why the hydrogen peroxide conversion efficiency does not increase directly proportional to energy dissipation. This may explain, why the lowest amount of energy dissipated generates the highest efficiency[28].
The hydrogen peroxide yield per pulse has a similar shape as the efficiency. Based on

these assumption, that the energy dissipated per pulse increases with treatment time, the yield should also increase. Therefore a steady increase of yield is to be expected. A paper by Wandell et al.[28] has researched a similar topic on efficiency and has come to a similar conclusion. They concluded, that the efficiency is decreasing over time and the production increases over time. They link this to the parallel increase in plasma temperature and electron density[28].

6.1 Outlook

The process of hydrogen peroxide production using microsecond pulsed plasmas, as well as the oxidization of copper surfaces and their subsequent crystalline copper oxides have been discussed and analyzed in detail and are in good accordance with other research papers discussing similar topics[31][28][16]. Yet there are still some interesting points worth discussing. For example the sudden rise in energy dissipated and temperature at 70 minutes treatment time and the copper oxide crystal growth patterns. A long treatment of water in order to increase hydrogen peroxide production may be impractical, as the hydrogen peroxide conversion efficiency drops with increasing treatment time and temperature of the water. This assumes shorter treatment times to be the most efficient at converting hydrogen peroxide. The nanosecond pulsed plasma indeed do have a higher rate of conversion[31], which is why nanosecond pulsed plasmas are more efficient in hydrogen peroxide production.
In conclusion, this thesis presented the changes of parameters on the usage of microsecond pulsed plasmas in liquid and the electrochemical data of cyclic voltammetry and the electron microscope images are in good accordance to similar research papers[31][16][12][28][32][33].

Danksagung

Zuletzt möchte ich mich bei allen ganz herzlich bedanken, die mir geholfen haben diese Masterarbeit zu schreiben. Ganz besonders bedanke ich mich bei

- Prof. Dr. Achim von Keudell, der mir die Möglichkeit gegeben hat, meine Arbeit an seinem Lehrstuhl zu schreiben und für die großartige Hilfe bei Fragen und Korrekturen.
- Prof. Dr. Judith Golda, die sich bereit erklärt hat, die Zweitkorrektur für meine arbeit zu übernehmen.
- Pia Pottkämper, für Ihre tolle Unterstützung und dafür, dass Sie während meiner gesamten Arbeit für ein angenehmes Arbeitsklima gesorgt hat.
- Steffen Schüttler, der mir den Absorptionsspektroskopie Aufbau gezeigt hat und bei meinen Aufnahmen geholfen hat.
- meinen Studiengefährten Oliver Krettek, Daniel Henze als auch Julia Sendt, durch die ich sehr viel Spaß im Studium gefunden habe.
- allen netten Arbeitskollegen, die ich kennenlernen durfte und mit denen ich schöne Mittagspausen verbracht habe.
- Lennart Kulik und Niklas Eichstaedt, gegen die ich viele Partien im Schach gewonnen habe.
- meinen Freunden und meiner Familie, die mich all die Jahre begleitet und unterstützt haben.

Literature

[1] Konstantinos C Christoforidis et al. “Photocatalysis for Hydrogen Production and CO2 Reduction: The Case of Copper-Catalysts”. In: *Chemistry Europe* (2018). DOI: 10.1002/cctc.201801198 (cit. on p. 1).

[2] Gong Zhang et al. “Electrochemical Approaches to CO2 Conversion on Copper-Based Catalysts”. In: *ACS Publications* (2023). DOI: 10.1021/accountsmr.2c00175 (cit. on p. 1).

[3] S. Horikoshi and N. Serpone. “In-liquid plasma: a novel tool in the fabrication of nanomaterials and in the treatment of wastewaters”. In: *Royal Society of Chemistry* (2017). DOI: 10.1039/C7RA09600C (cit. on pp. 3, 4).

[4] Jannis Teunissen Sander Nijdam and Ute Ebert. “The physics of streamer discharge phenomena”. In: *IOP Science* (2020). DOI: 10.1088/1361-6595/abaa05 (cit. on pp. 3, 4).

[5] Prof. A. von Keudell. “Einführung in die Plasmaphysik”. In: (2024) (cit. on p. 3).

[6] N Skoro et al. “Electrical Breakdown in Water Vapor”. In: *American Physical Society* (2011). DOI: 10.1103/PhysRevE.84.055401 (cit. on pp. 3, 29).

[7] Peter Bruggeman and Christophe Leys. “Non-thermal plasmas in and in contact with liquids”. In: *IOP Science* (2009). DOI: 10.1088/0022-3727/42/5/053001 (cit. on p. 4).

[8] Fatma-Nur Seferoglu. “Optical Analysis of Microsecond Pulsed Plasmas in Liquids”. In: *Private* (2022) (cit. on pp. 4, 16, 34).

[9] Hidesama Fujita. “Initiation process and propagation mechanism of positive streamer discharge in water”. In: *AIP Publishing* (2014). DOI: 10.1063/1.4902862 (cit. on pp. 5, 29).

[10] Rohit Thirumdas et. al. “Plasma activated water (PAW): Chemistry, physico-chemical properties, applications in food and agriculture”. In: *Trends in Food Science and Technology* (2018). DOI: 10.1016/j.tifs.2018.05.007 (cit. on p. 6).

[11] “Components of Air”. In: (2025) (cit. on p. 5).

[12] D. DeNardis. “Characterization of copper-hydrogen peroxide film growth kinetics”. In: *sciencedirect* (2006). DOI: 10.1016/j.tsf.2006.02.010 (cit. on pp. 6, 7, 57, 59).

[13] D. DeNardis. “Studying the effect of temperature on the copper oxidation process using hydrogen peroxide for use in multi-step chemical mechanical planarization models”. In: *sciencedirect* (2006). DOI: 10.1016/j.tsf.2009.12.089 (cit. on pp. 6–8).

[14] N Barera et al. “Theory of the oxidation of metals”. In: *IOPScience* (1949). DOI: 10.1088/0034-4885/12/1/308 (cit. on p. 6).

[15] Frank Marken. “Electroanalytic Methods, Cyclic Voltammetry”. In: *Springer Nature* (2009). DOI: 10.1007/978-3-642-02915-8_4 (cit. on p. 9).

[16] H Gil. “Electrochemical reduction modeling of copper oxides obtained during in situ and ex situ conditions in the presence of acetic acid”. In: *ScienceDirect* (2009). DOI: 10.1016/j.electacta.2009.03.082 (cit. on pp. 9, 10, 49, 57, 59).

[17] Paul A. Ciguere M.K. Phibbs. “HYDROGEN PEROXIDE AND ITS ANALOGUES: III. ABSORPTION SPECTRUM OF HYDROGEN AND DEUTERIUM PEROXIDES IN THE NEAR ULTRAVIOLET”. In: *Canadian Science publishing* (1951). DOI: 10.1139/v51-058 (cit. on p. 9).

[18] Daniele Suzzi Stefan Radl Silvia Larisegger and Johannes G. Khinast. “Quantifying Absorption Effects during Hydrogen Peroxide Decontamination”. In: *Journal of Pharmaceutical Innovation* (2011). DOI: 10.1007/s12247-011-9114-6 (cit. on p. 9).

[19] W. Paterlini R. Nogueira M. Oliveira. “Simple and fast spectrophotometric determination of H2O2 in photo-Fenton reactions using metavanadate”. In: *Talanta, Volume 66, Issue 1* (2005). DOI: 10.1016/j.talanta.2004.10.001 (cit. on p. 10).

[20] Avin Abdullah Azad Mohammed. “Scanning Electron Microscopy (SEM): A Review”. In: *Proceedings of 2018 International Conference on Hydraulics and Pneumatics - HERVEX* (2018). DOI: ISSN1454-8003 (cit. on pp. 11, 12).

[21] K D Vernon Parry. “Scanning electron microscopy: an introduction”. In: *Elsevier, ScienceDirect* (2000). DOI: 10.1016/S0961-1290(00)80006-X (cit. on p. 11).

[22] Sharbaugh and Devins. “PROGRESS IN THE FIELD OF ELECTRIC BREAKDOWN IN DIELECTRIC LIQUIDS”. In: *General Electric Research and Development Center Schenectady* (1978). DOI: 10.1109/TEI.1978.298076 (cit. on pp. 16, 36, 37).

[23] LH Dawsey HC Urey. “The absorption spectrum and decomposition of hydrogen peroxide by light”. In: *ACS Publications* (1929). DOI: 10.1021/ja01380a011 (cit. on p. 18).

[24] Masuhiro Kogoma. “Low-temperature atmospheric discharge plasma and its applications for the surface treatment”. In: *Reviews of modern plasma Physics, Springer Nature Link* (2021). DOI: 10.1007/s41614-021-00050-4 (cit. on p. 24).

[25] Johannes Staehelin. “Decomposition of Ozone in Water: Rate of Initiation by Hydroxide Ions and Hydrogen Peroxide”. In: *PUBS ACS* (1982). DOI: 10.1021/es00104a009 (cit. on p. 26).

[26] H L Penman. “Estimating evaporation”. In: *Advanced Earth and Space sciences* (1956). DOI: 10.1029/TR037i001p00043 (cit. on p. 26).

[27] Berger. “Dielectric strength of insulating materials”. In: *mdma.ch* (2006) (cit. on p. 29).

[28] Huihui Wang Robert Wandell. “Nanosecond pulsed plasma discharge over a flowing water film: Characterization of hydrodynamics, electrical, and plasma properties and their effect on hydrogen peroxide generation”. In: *Wiley online library* (2018). DOI: 10.1002/ppap.201800008 (cit. on pp. 40, 58, 59).

[29] Tadahiko Mizuno et al. “Production of Heat during Plasma Electrolysis in Liquid”. In: *IOP Science* (2000). DOI: 10.1143/JJAP.39.6055 (cit. on pp. 41, 42).

[30] Merck. “Hydrogen Peroxide test kit”. In: *Merck milipore com* (2025). DOI: https://www.merckmillipore.com/DE/de/product/Hydrogen-Peroxide-Test,MDA_CHEM-118789 (cit. on p. 45).

[31] Laura Chauvet, Katharina Grosse, and Achim von Keudell et al. “Chemistry in nanosecond plasmas in water”. In: *Wiley online library* (2020). DOI: 10.1002/ppap.201900192 (cit. on pp. 46, 58, 59).

[32] Adair Gallo Jr et al. “On the formation of hydrogen peroxide in water microdroplets”. In: *Royal society of chemistry* (2022). DOI: 10.1039/d1sc06465g (cit. on pp. 47, 59).

[33] N Ichikawa et al C C Lin. “Decomposition of hydrogen peroxide in aqueous solutions at elevated temperatures”. In: *Chemical kinetics* (1991). DOI: 10.1002/kin.550231103 (cit. on pp. 47, 58, 59).

[34] A Vvendeskii and S Grushevskaya et al. “Copper oxides: kinetics of formation and semiconducting properties. Part II. Copper single crystals”. In: *Springer Nature Link* (2014). DOI: 10.1007/s10008-014-2569-x (cit. on p. 51).

[35] Kenneth R Lawless and Allan T Gwathmey. “The structure of oxide films on different faces of a single crystal of copper”. In: *ScienceDirect* (1956). DOI: 10.1016/0001-6160(56)90133-X (cit. on pp. 51, 52, 57).